Modifiable Stability and Maneuverability of High Speed Unmanned Underwater Vehicles (UUVs) Through Bioinspired Control Fins

by
Nastasia Elizabeth Winey
B.S., Johns Hopkins University, 2017
Submitted to the Joint Program in Applied Ocean Science & Engineering
in partial fulfillment of the requirements for the degree of
Masters of Science
at the
MASSACHUSETTS INSTITUTE OF TECHNOLOGY
and the
WOODS HOLE OCEANOGRAPHIC INSTITUTION
September 2020

Author .....
Joint Program in Oceanography/Applied Ocean Science and Engineering
Massachusetts Institute of Technology
and Woods Hole Oceanographic Institution
August 7, 2020

Certified by .....
Michael Triantafyllou
Henry L. and Grace Doherty Professor in Ocean Science and Engineering
Massachusetts Institute of Technology
Thesis Supervisor

Certified by .....
Dana Yoerger
Senior Scientist
Woods Hole Oceanographic Institution
Thesis Supervisor

Accepted by .....
Nicolas Hadjiconstantinou
Chairman, Committee for Graduate Students
Massachusetts Institute of Technology

Accepted by .....
David Ralston
Chairman, Joint Committee for Applied Ocean Science & Engineering
Massachusetts Institute of Technology/
Woods Hole Oceanographic Institution

Modifiable Stability and Maneuverability of High Speed Unmanned Underwater Vehicles (UUVs) Through Bioinspired Control Fins

by

Nastasia Elizabeth Winey

Submitted to the Joint Program in Oceanography/Applied Ocean Science and Engineering
Massachusetts Institute of Technology
and Woods Hole Oceanographic Institution
on August 7, 2020, in partial fulfillment of the
requirements for the degree of
Masters of Science

Abstract

Underwater Vehicles generally have control fins located only near their aft end, for making controllable changes in directions. This design allows for stability of control; however, the turns are typically large in comparison to the vehicle body length. Some bony fish, such as tuna, on the other hand, have deployable ventral and dorsal fins located towards the front of their body, in addition to their other fins. Their deployable fins allow them to modulate their hydrodynamic behavior in response to their environment. Tunas keep these fins retracted during steady cruising, and then deploy them during rapid maneuvers. However, the details of these hydrodynamic effects are not well understood. To investigate this phenomena, using a REMUS 100 as a model, a pair of vertical fins was added at different hull positions, to investigate the effects of fin location on the horizontal plane hydrodynamics, through: stability parameters, nonlinear simulation, and towing tank experiments. Depending on the added fin location, the stability of the vehicle changed, thereby affecting the maneuverability. As fins were placed further forward on the vehicle, maneuverability increased, with effects tapering off at 0.2 BL ahead of the vehicle's center of buoyancy. This investigation explored how rigid underwater vehicles could benefit from added fins, without drastically changing the design of current vehicles.

Thesis Supervisor: Michael Triantafyllou
Title: Henry L. and Grace Doherty Professor in Ocean Science and Engineering
Massachusetts Institute of Technology

Thesis Supervisor: Dana Yoerger
Title: Senior Scientist
Woods Hole Oceanographic Institution

Biography

Acknowledgments

First, I would like to thank my Advisors, Professor Michael Triantafyllou, Head of MIT's Sea Grant, and Dr. Dana Yoerger, Senior Scientist of WHOI. Without their guidance and encouragement, it would have been difficult to achieve my results. I would like to thank my labmates, Yuri Trakht, and Raz Elhassid who aided my research efforts, as well as Dixia Fan, Miranda Kotidis, and Brian Gilligan who offered support throughout my time. I must offer my thanks to my friends and family who have aided me throughout my journey, both before and at MIT. Lastly, I would like to thank Lockheed Martin for funding this work. I would also like to mention that some of the results of this work have been published in the journal of *Bioinspiration and Biomimetics* [15].

Contents

List of Figures

List of Tables

Chapter 1

Introduction

Highly maneuverable UUVs are desirable for doing exploration around areas with tight bends, and obstacles. Stable, low maneuverability vehicles are desirable when steady, level motions are critical, as when performing side-scan surveys. Each type of vehicle has its uses, often in the same mission, and one vehicle cannot typically perform both tasks adequately, requiring multiple vehicles for the different tasks. Additionally, most vehicles are not highly maneuverable. Those that have been created, use designs based off of the powerful tails of fish [10, 17, 16], or jets placed periodically around the vehicle [11]. All of these designs require higher order controllers, more expensive actuation, or are not stable or operable at fast speeds. For optimal performance during missions, a single UUV needs to have the ability to be either maneuverable or more stable, depending on the requirement of the mission. To achieve this, the stability must be modifiable.

1.1 Motivation

Having low-cost unmanned underwater vehicles (UUVs) are a critical need for more effectively monitoring and researching the ocean, particularly for high risk of loss missions, such as under the arctic ice. Some UUVs can cost millions of dollars, making owners wary to use them when the risk of loss is so high. Without mitigation, M. Brito et al.'s expert driven risk analysis software predicted the chance of loss of an Autosub3 AUV for a multitude of missions at Pine Island Glacier, Antarctica. They found a 29%-72% chance of loss for the Autosub3 AUV, depending on the duration of missions under the sea ice, the ice shelf, or in open water. They were able to use mitigation techniques to bring the risk to below 23%

for all mission types [2], however this may not be possible for all vehicles. Additionally, as the cost of the vehicle increases, the risk users are willing to take for operations decreases. Having a cheaper vehicle, or a multitude of cheaper vehicles, to deploy to collect data would help users be less averse to the loss. However, this is not the only requirement to deploy more vehicles and collect data. Missions with areas of high risk can also include obstacle ridden waters, such as floating ice, requiring quick maneuvering to avoid. The ideal research or survey vehicle would require both.

Current low cost vehicles that do exist, in the commercial industry, have limited mobility and battery life, which narrows the scope of missions that can be achieved. Novel, maneuverable vehicles that make use of the tail design of fish are unlikely to be adopted by industry, because of their significant change in design and control, which does not currently scale well to mass production, making it unlikely to become an option for the general public. Additionally, making use of a flapping tail for motion, leads to an oscillatory motion, that is less than ideal for taking video and performing scans [10], and also makes the vehicle less stable. Therefore, it is desirable to look for novel methods to increase the capabilities of vehicles, but not at the cost of stability, and without drastically changing the typical torpedo style design of low cost UUVs. This would allow for an ease of transition into manufacturing, without increasing the cost, which would allow for it to be more cost effective and efficient to deploy vehicles in these high risk areas and gather back meaningful data.

1.2 Models

1.2.1 Biological Model

Rigid UUVS are the most common design in industry, however, without the ability of the hull to flex, it is difficult to make tight turns, as many have a turning radius of several body lengths, while in world of biology, angel fish can turn in as little as 0.065 body lengths [4], partially because they can curl up their entire body. However, bony fish, such as tuna have greatly reduced flexibility in comparison to their cousins. Despite this, they are some of nature's quickest and most agile swimmers. Yellowfin tuna, for example, have a turning radius of 0.47 ± 0.18 body lengths [1]. One contributor to their performance is, to compensate for their lack of flexibility, they have deployable fins. Pavlov et al. [12] found that the Pacific bluefin tuna and yellowfin tuna have extendable fins controlled by their lymphatic system.

Through adaptation, they use their lymphatic system to contract the muscles surrounding the lymph nodes to force fluid into their second dorsal and anal fins, causing them to rise out of the body as seen in image A of figure 1-1. With their fins deployed, they are able to maneuver around, turning rapidly to catch prey. Once the muscles relax, the fins retract partially back into their body, as seen in image B of figure 1-1. This second behavor is observed during steady swimming. Additionaly, during steady swimming, the first dorsal fin is observed to be completely compressed into the body [12]. While observed in video, no such studies been performed to understand the affect of their deployable dorsal and anal fins, hydrodynamically. It has been shown though, that the faster these fish swim in a straight line, the closer they choose to hold their pectoral fins into their body [6], hinting that their could be a simlar function for their deployable fins.

Several studies have been conducted on using a tuna fish's tail in vehicles for the propulsion of more maneuverable vehicles [10, 17, 16], however non have been made for understanding the effect of pop-up fins on vehicle maneuverability. If a simple pop-up added fins such as that found on tuna, were applied to UUVs, then the stability and therefore the maneuverability could be modular, to have stability when going straight and level, without the fins, and with the fin deployed, lower stability and a smaller turning radius. A simple added fin would also be a cheaper change in UUV design, than an entire overhaul in vehicle design. However, before making these adaptations, these observations need to be verified. In this study, the position of an added fin is tested, to see whether an extra fin does indeed, affect the maneuverability of UUVs, and if there is an optimal placement for this extra control fin.

In addition to their evolutionary deployable fins, tunas also make a good biological models for UUVs due to their relatively rigid bodies, and similar size and speed profiles to UUVs. Bluefin tuna range between .5 m and 3.5 m in size and swim between 0.8 m/s and 1.6 m/s [3], while the smaller yellowfin tuna, averaging at 0.3 m, has been observed to swim between 0.49 and 1.25 m/s [6]. This size and speed range, falls within the bounds of typical UUVs, such as the REMUS 100 AUV which is 1.33 m in length and operates at 1.5 m/s.

1.2.2 Description of Vehicle

The vehicle model used is the REMUS 100 AUV, a torpedo shaped vehicle with a cruciform rudder configuration on the aft end of the vehicle. For all future references, the REMUS 100 will be abreviated as just the REMUS. The REMUS is similar in build to low cost

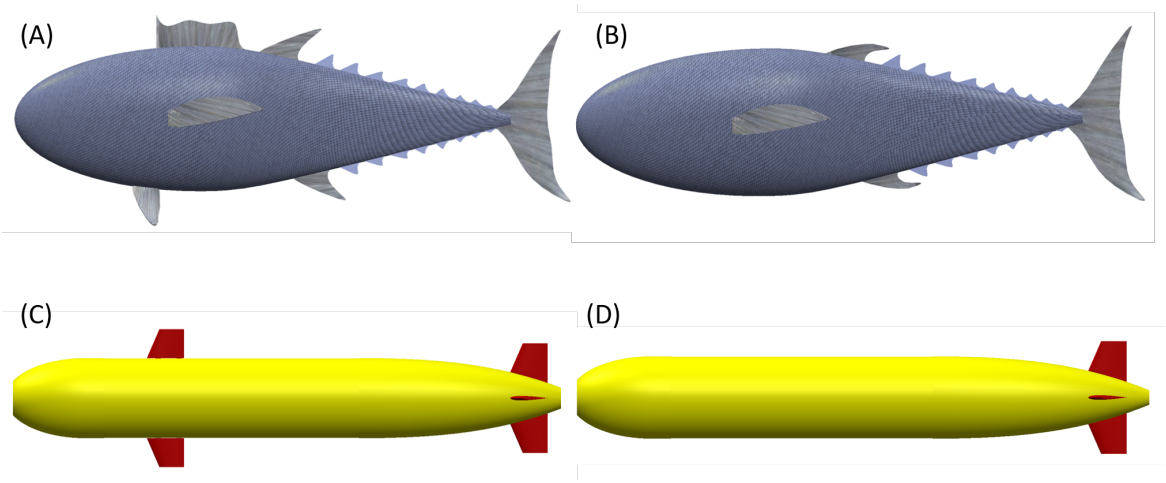

Figure 1-1: Visualization of adapting the deployable fins of tuna to the REMUS. (A) The tuna with its first and second dorsal fins, pelvic fins, and anal fins deployed, (B) shows the same tuna with pelvic and first dorsal fins fins tucked into the body, and the second dorsal and anal fins partly retracted. to mimic this feature in a REMUS AUV, an added pair of fins would be added to the vehicle (C), that could be retracted, to return the vehicle to its original configuration (D) for a simple 2-state fin configuration. Additionally, when retracted these added fins do not add any constraints for launching or recovering the vehicle.

UUVS commercially available, and has had simulation and physical experimentation already performed, to use for comparison and validation [13]. For this work, the REMUS's low-frequency sonar transducer, which is a bluff body attached to the hull, will be discarded. The focus of this research will be on added control fins on streamlined bodies, and the sonar transducer as a buff body reduces this effect, and would change flow over the added control fins. In terms of added fins, in the tuna model, the fish have deployable dorsal fins 2/3 down the body from the head. However, it is not known whether this location is the best location. This research endeavor will look to find the best location, by testing added fins at different points on the body. This work will assume the transient time of the fin deploying is unimportant for the overall behavior of the vehicle, and will therefore only investigate when a rigid added fin is fully deployed as in image C of figure 1-1 to the original vehicle in image D of 1-1.

1.3 Chapter Layout

Chapter two will derive the hydrodynamic coefficients that control the dynamics of the vehicle in the horizontal plane, both for the original vehicle, and for one with added fins.

Chapter three will define stability and maneuverability, and will use the derived hydrodynamic coefficients to evaluate this behavior through simulations. chapter four describes static and dynamic experiments conducted in the MIT towing tanks to find the hydrodynamic coefficients experimentally to compare to the theoretical stability results of chapter three. Chapter five Discusses changes to improve the maneuverability of the vehicle further as well as details initial vehicle tests and future steps.

Chapter 2

Hydrodynamic Theory

Hydrodynamic theory was used to develop hydrodynamic coefficients for the REMUS, which can be used to predict the response of the vehicle to different inputs. For the scope of this work, only the behavior of the vehicle in the horizontal plane was investigated, and so only the horizontal plane forces, moment, and velocities were needed. The vehicle follows a right handed coordinate system, as shown in figure 2-1 with the positive x-axis aligned with the body axis, in the direction of the nose. By the right hand rule, the positive Y direction is aligned towards the right of the body, such that the positive z-axis is oriented down into the ocean floor. The forces and velocities of this system follow SNAME notation, with the x-axis force represented by X, the y-axis force by, Y, and the rotational moment about the z-axis, as N, and their velocities as u, v, and angular velocity r, respectively [5]. All acceleration terms are represented using the dot notation over the velocity terms, such as $\dot{u}$ to represent forward acceleration. The origin of this coordinate frame is centered at the center of buoyancy (CoB) of the vehicle, as this value tends to remain constant during the life of the vehicle, while the center of gravity can change between missions as the payload changes.

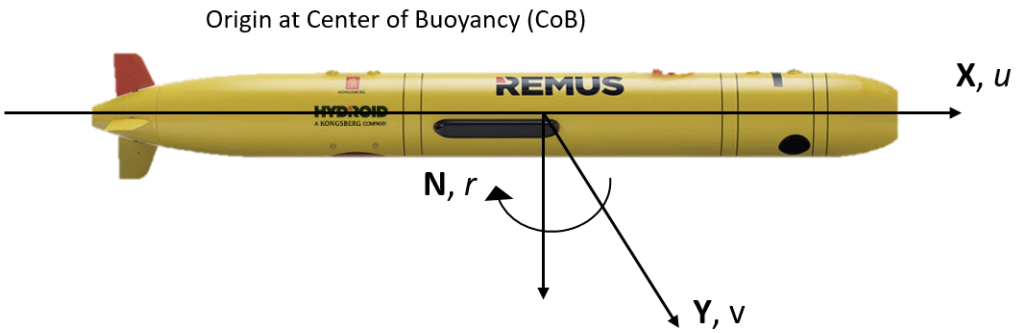

Figure 2-1: Coordinate frame of the REMUS UUV

2.1 Vehicle Geometry

2.1.1 Hull Geometry

The hull profile of the REMUS UUV is represented by the Myring profile equations found by Prestero [13]. The radius, r, of the nose profile, is given by

$$r = \frac{1}{2}d\Big\{1 - \Big(\frac{x + x_{0n} - a}{a}\Big)^2\Big\}^{\frac{1}{n}} \tag{2.1}$$

where, d, is the maximum diameter of the hull, a, is the length of the nose if the vehicle had a full semi-ellipsoid shaped nose of the same profile, n, is the nose index for the curve of the nose, and x_{0n}, is the offset needed to translate the equation to align with the vehicle coordinate frame. For the tail, the radius, r, is given by

$$r = \frac{1}{2}d - \Big\{\frac{3d}{2c^2} - \frac{tan(\alpha)}{c}\Big\}(x + x_{0t} - l)^2 + \Big\{\frac{d}{c^3} - \frac{tan(\alpha)}{c^2}\Big\}(x + x_{0t} - a - b + a_{offset})^3 \tag{2.2}$$

where, b, is the body's straight section length, c, is the tail length, α, is the tail semi angle, and x_{0t}, is the offset needed to translate the equation to align with the vehicle coordinate frame. Lastly, a_{offset}, is the length of the semi-ellipsoid shaped nose, with length, a, that needs to be cut off to produce the flat face of the vehicle that is present. All of these variables are labeled in figure 2-2 and the values indicated in table 2.1 [13]. The body of the vehicle has a constant radius, equal to half of the maximum diameter, d. The bounds for each of the sections of the hull are given in table 2.2.

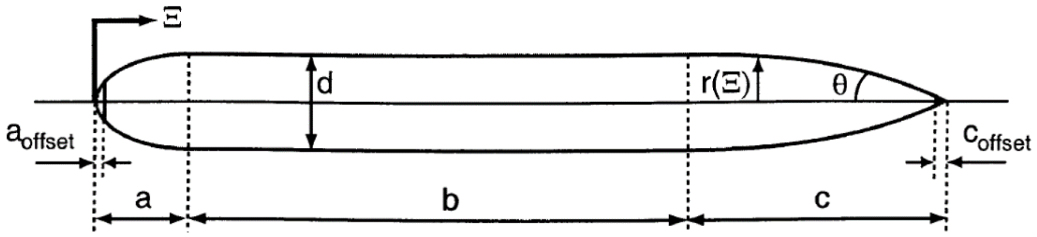

Figure 2-2: Standard Myring hull profile with variables [13]

Table 2.1: Geometry of the REMUS body [13]

variable	value	meaning
d	0.191 m	hull diameter
n	2	nose index
l	1.33 m	vehicle length
a	0.191 m	nose length
b	0.654 m	body length
c	0.541 m	tail length
α	0.436	tail semi-angle
x_{0n}	-0.2625	nose equation offset
x_{0t}	1.0465	tail equation offset
x_G	-0.412 m	horizontal distance from nose to center of gravity
x_{CoB}	-0.611 m	horizontal distance from nose to center of Buoyancy

The vehicle has a mass, m, of 30.5 kg and with the afformentioned geometry, the moment of Inertia, I_{zz}, is 3.45 kgm^2.

Table 2.2: Locations of important geometric features of the REMUS

Variable	meaning	value(m)
x_{b2}	tip of vehicle nose	0.61
x_b	end of nose section and start of body section	0.437
x_{t2}	start of tail section and end of body section	-0.218
x_{f2}	start of fin section	-0.578
x_f	end of fin section	-0.668
x_t	end of vehicle and end of tail section	-0.721

2.1.2 Control Surface Geometry

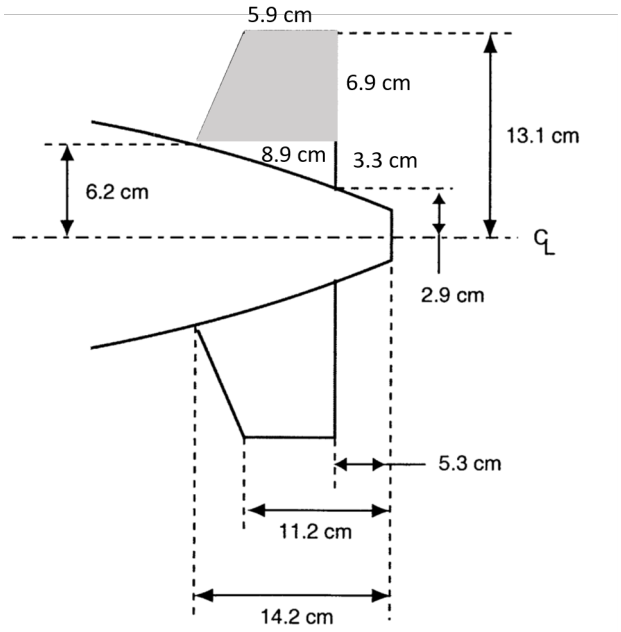

Figure 2-3: Dimensions of the control surfaces of the REMUS. The entire control surface is the rudder, the shaded region is the chosen area of the added fins

The REMUS has four rudders in a cruciform configuration on the tail. The rudder's profile design is shown in figure 2-3, with the geometric parameters listed in table 2.3. The added fins are modeled off of the rudder's design for simplicity, consisting of an exact replica of the upper trapezoidal region of the rudder, as seen by the shaded region of figure 2-3. They are located anywhere between 0.25 m and -0.25m along the hull, depending on the case being investigated. The bounds for the location of the fins were chosen so that the fins would only be positioned along the body section of the hull, as they would be the easiest to test

Table 2.3: Rudder and added fin geometry

variable	value	meaning
x_{rud}	-0.6312 m	location of the rudder on the hull
b_r	0.171 m	paired rudder span height
S_{rud}	0.00657 m^2	rudder area (1/2 fin pair)
a_{rud}	0.131 m	max rudder height above center line
$\bar{a}$	0.9 rad	lift slope parameter
AR_r	2.2253	rudder aspect ratio
t	0.654	rudder taper ratio
b_f	0.138 m	paired added fin span height
S_{fin}	0.0051 m^2	rudder area (1/2 fin pair)
a_{fin}	0.2335 m	max rudder height above center line
AR_f	1.8649	fin added fin aspect ratio

experimentally. For both types of control fins, an important parameter is the aspect ratio, AR, of the control surface.

$$AR = \frac{b_{fin}^2}{S_{fin}} \tag{2.3}$$

where b_{fin} is the span of the fin pair and S_{fin} is the area of a single fin of the pair.

2.2 Lift

The lift of the vehicle, causing the body to turn, is broken up into the lift from the body, and the lift generated from the control surfaces. This fin driven lift, will be the major variant among the hydrodynamic coefficients for affecting how the vehicle will behave with added control fins on the body.

2.2.1 Control Surface Lift

The general form for lift generated by the control surface, L_{rud}, is

$$L_{rud} = \frac{1}{2}\rho C_L(2S_{rud})v_e^2 \tag{2.4}$$

where, ρ, is the density of the water [13]. The density of freshwater, at 1000 kg/m^3 was used, because despite the vehicle operating in sea-water, which has a density more strongly dependent on temperature, the difference in value is insignificant. It will also, make

comparison to the experiments performed in freshwater easier. C_L, is the lift coefficient for the rudder, and, v_e, is the effective rudder velocity [13]. The effective velocity come from the rudder being offset from the origin of the vehicle, causing the rudder's velocity and angle of attack to be different from the vehicle origin, with respect to water flow. The velocity of the rudder, v_e, observes is,

$$\begin{aligned} v_e &= (u_{rud}, v_{rud}) \\ u_{rud} &= u \\ v_{rud} &= v + x_{rud} r \end{aligned} \tag{2.5}$$

where x_{rud}, is the location of the rudder on the hull, through which the forces of the rudder act.

The lift coefficient, C_L, of the rudder, varies with the aspect ratio and effective angle of attack, δ_e of the rudder [8].

$$C_L = \frac{dC_L}{d\delta_e}\delta_e \tag{2.6}$$

where,

$$\frac{dC_L}{d\delta_e} = \frac{1}{\frac{1}{2\bar{\alpha}\pi} + \frac{1}{\pi(AR)} + \frac{1}{2\pi(AR)^2}} \tag{2.7}$$

is the equation to determine the lift coefficient for a fin, were $\bar{\alpha}$ is the lift slope parameter [14]. The effective angle of the rudder, δ_e, is

$$\delta_e = \delta_r - \beta_{re} \tag{2.8}$$

where, δ_r, is the rudder angle commanded to the vehicle, and, β_{re}, is the modification factor, resulting from the effective velocity of the rudder not being the same as the forward velocity of the vehicle, resulting in

$$\beta_{re} = tan^{-1}\frac{v_{rud}}{u_{rud}} \tag{2.9}$$

Small angle approximation yields

$$\beta_{re} = \frac{v_{rud}}{u_{rud}} \tag{2.10}$$

Putting all of these components together, and discounting v_{rud} terms higher than order 1, due to its small value in comparison to u_{rud}, yields

$$L_{rud} = \rho c_{L\delta_e} S_{rud}(\delta_r u^2 - uv - x_{rud} ru) \tag{2.11}$$

This force is in y-direction and moment of this lift is calculated by multiplying L_{rud}, by the location of the rudder, x_{rud}. The lift force can be broken into nonlinear hydrodynamic components by taking the derivative of this force with respect to the input, δ_r and the velocity terms, until only the constant terms remain.

$$Y_{u^2\delta_r} = \rho c_{L\alpha} S_{rud} \tag{2.12}$$

$$Y_{uv_r} = -\rho c_{L\alpha} S_{rud} \tag{2.13}$$

$$Y_{ur_r} = -\rho c_{L\alpha} S_{rud} x_{rud} \tag{2.14}$$

$$N_{u^2\delta_r} = \rho c_{L\alpha} S_{rud} x_{rud} \tag{2.15}$$

$$N_{uv_r} = -\rho c_{L\alpha} S_{rud} x_{rud} \tag{2.16}$$

$$N_{ur_r} = -\rho c_{L\alpha} S_{rud} x_{rud}^2 \tag{2.17}$$

where the subscripts following Y or N indicate which partial derivative were taken, and the subscript, r, on the subscript indicates that these terms relate to the rudder specifically. The derivation for the added fins follows the same format relayed in this section, but with the all variables with subscript "rud" replaced with "fin."

2.2.2 Body Lift

The general equation for body lift, L_{body}, follows a similar format to that for control surfaces.

$$L_{body} = -\frac{1}{2}\rho d^2 c_{yd} U^2 \text{ [13]} \tag{2.18}$$

where the body lift coefficient, c_{yd}, is calculated using Hoerner [8].

$$c_{yd} = c_{yd}(\beta) = \frac{dc_{yd}}{d\beta}\beta \tag{2.19}$$

where, β, is the drift angle of the vehicle in radians, and $\frac{dc_{yd}}{d\beta}$ is relationship between the lift coefficient and β, calculated as

$$\frac{dc_{yd}}{d\beta} = (\frac{l}{d})c^{\circ}_{y\beta}\frac{180}{\pi} \tag{2.20}$$

where $c_{y\beta^{\circ}}$, is a parameter that depends on the vehicle length to diameter ratio. When this ratio is between 6.7 and 10, as is the case for this vehicle

$$c_{y\beta^{\circ}} = \frac{0.003}{\circ} \text{ [8]} \tag{2.21}$$

The drift angle, β for the horizontal plane, comes from the vehicle having a side slip velocity, v, instead of always moving purely forward, leading to

$$tan(\beta) = \frac{v}{u} \tag{2.22}$$

which can be simplified for angles less than 10° as

$$\beta = \frac{v}{u} \tag{2.23}$$

Combining all of these terms yields a body force,

$$L_{body} = -\frac{1}{2}\rho d^2(\frac{l}{d})0.003(\frac{180}{\pi})vU \tag{2.24}$$

The associated moment, is achieved by multiplying the lift force by where it acts along the body, which is the center or pressure of the vehicle, x_{cp}. Hoerner has estimated the center of pressure to occur between 0.6 and 0.7 of the body length with respect to the vehicle nose [8]. Here the average of those two values is used, and then the resulting value is converted to be in the body coordinate frame, centered at the CoB.

$$x_{cp} = 0.65l - x_{CoB} \tag{2.25}$$

breaking this force down into the nonlinear hydrodynamic coefficients,

$$Y_{uv_b} = -\frac{1}{2}\rho d^2(\frac{l}{d})0.003(\frac{180}{\pi}) \tag{2.26}$$

$$N_{uv_b} = Y_{uv_b}x_{cp} \tag{2.27}$$

where the subscript b on the subscripts indicate that these terms come from the REMUS body.

2.3 Added Mass

The vehicle has added mass coefficients, associated with the vehicle moving the water around it as it accelerates. With no symmetry, the general added mass matrix is

$$\begin{bmatrix} X_{\dot{u}} & X_{\dot{v}} & X_{\dot{r}} \\ Y_{\dot{u}} & Y_{\dot{v}} & Y_{\dot{r}} \\ N_{\dot{u}} & N_{\dot{v}} & N_{\dot{r}} \end{bmatrix} \tag{2.28}$$

The Remus has xy-plane symmetry, reducing the added mass matrix to

$$\begin{bmatrix} X_{\dot{u}} & 0 & 0 \\ 0 & Y_{\dot{v}} & Y_{\dot{r}} \\ 0 & N_{\dot{v}}0 & N_{\dot{r}} \end{bmatrix} \tag{2.29}$$

Using the Kirchhoff's energy equations, one can find the crossflow added mass terms, by simplifying out terms that are zero, using this symmetry [5]. In the x-direction

$$\begin{aligned} X &= X_{\dot{u}}\dot{u} + X_{\dot{v}}(\dot{v} - ur) + X_{\dot{r}}\dot{r} - Y_{\dot{v}}vr - Y_{\dot{r}}r^2 \\ &= X_{\dot{u}}\dot{u} + \cancel{X_{\dot{v}}(\dot{v} - ur)} + \cancel{X_{\dot{r}}\dot{r}} - Y_{\dot{v}}vr - Y_{\dot{r}}r^2 \\ &= X_{\dot{u}}\dot{u} - Y_{\dot{v}}vr - Y_{\dot{p}}pr - Y_{\dot{r}}r^2 \end{aligned} \tag{2.30}$$

the remaining coefficients were renamed to match the force direction under investigation, with subscripts to match the variables following the coefficients. These coefficients are set

equal to the original coefficient name, and are used for calculating the coefficient value.

$$X_{\dot{u}} = X_{\dot{u}}$$
$$X_{vr} = -Y_{\dot{v}}$$
$$X_{rr} = -Y_{\dot{r}}$$
$$X_{\dot{v}} = X_{\dot{r}} = X_{ur} = X_{wr} = 0$$

In the y-direction,

$$\begin{aligned} Y &= X_{\dot{v}}(\dot{u} + ur) + Y_{\dot{v}}\dot{v} + Y_{\dot{r}}\dot{r} + X_{\dot{r}}r^2 + X_{\dot{u}}ur \\ &= \cancel{X_{\dot{v}}(\dot{u} + ur)} + Y_{\dot{v}}\dot{v} + Y_{\dot{r}}\dot{r} + \cancel{X_{\dot{r}}r^2} + X_{\dot{u}}ur \\ &= Y_{\dot{v}}\dot{v} + Y_{\dot{r}}\dot{r} + X_{\dot{u}}ur \end{aligned} \tag{2.31}$$

leaving,

$$Y_{\dot{v}} = Y_{\dot{v}}$$
$$Y_{\dot{r}} = Y_{\dot{r}}$$
$$Y_{ura} = X_{\dot{u}}$$
$$Y_{\dot{u}} = 0$$

Finally, for the horizontal moment, N

$$N = X_{\dot{r}}\dot{u} + X_{\dot{v}}u^2 + Y_{\dot{r}}\dot{v} + N_{\dot{r}}\dot{r} - X_{\dot{v}}v^2 - X_{\dot{r}}vr - X_{\dot{u}}uv + Y_{\dot{v}}uv + Y_{\dot{r}}ur$$

$$N = \cancel{X_{\dot{r}}\dot{u}} + \cancel{X_{\dot{v}}u^2} + Y_{\dot{r}}\dot{v} + N_{\dot{r}}\dot{r} - \cancel{X_{\dot{v}}v^2} - \cancel{X_{\dot{r}}vr} - X_{\dot{u}}uv + Y_{\dot{v}}uv + Y_{\dot{r}}ur \tag{2.32}$$

$$= Y_{\dot{r}}\dot{v} + N_{\dot{r}}\dot{r} - X_{\dot{u}}uv + Y_{\dot{v}}uv + Y_{\dot{r}}ur \tag{2.33}$$

leaving,

$$N_{\dot{v}} = Y_{\dot{r}}$$

$$N_{\dot{r}} = N_{\dot{r}}$$

$$N_{uva} = -X_{\dot{u}} + Y_{\dot{v}}$$

$$N_{ura} = Y_{\dot{r}}$$

$$N_{\dot{u}} = N_{uu} = N_{vv} = N_{vr} = 0$$

For both Y and N, the terms involving, a, in the subscript pertain to the Munk moment, and should be calculated neglecting the effect of the control surfaces.

2.3.1 Computing Added Mass

Strip theory for slender bodies can be used to obtain every added mass coefficient, except $X_{\dot{u}}$, as the force is parallel to the length of the body, and strip theory only works for forces perpendicular. The coefficients are also symmetric over the diagonal of the added mass matrix, resulting in

$$\begin{bmatrix} X_{\dot{u}} & 0 & 0 \\ 0 & m_{22} = \int_L -M_{22}dx & m_{26} = \int_L -xM_{22}dx \\ 0 & m_{62} = \int_L -xM_{22}dx & m_{66} = \int_L -x^2M_{22}dx \end{bmatrix} \tag{2.34}$$

where M_{22} is the added mass for a thin 2D cross section of the vehicle to be integrated over the length of the vehicle [9]. For the majority of the vehicle, the 2D cross section is a circle, with added mass,

$$M_{22} = \pi\rho R(x)^2 \tag{2.35}$$

and for the sections of the vehicle that include control surfaces, this becomes

$$m_{22} = \pi\rho(a_{fin}^2 - R(x)^2 + \frac{R(x)^4}{a_{fin}^2}) \tag{2.36}$$

where a_{fin} is the maximum height of the fin above the centerline [9].

The surge added mass, $X_{\dot{u}}$, was determined using Fossen and assuming the hull is an

ellipsoid,

$$X_{\dot{u}} = -\frac{\alpha_0}{2-\alpha_0} m_{ps} \tag{2.37}$$

where, α_0, is a constant, and m_{ps} is the mass of a prolate spheroid, calculated as

$$m_{ps} = \frac{4}{3}\pi\rho h d^2 \tag{2.38}$$

where, h, is the half-length of the vehicle. To constant, α_0, is calculated through

$$\alpha_0 = \frac{2(1-e^2)}{e^3}(\frac{1}{2} ln \frac{1+e}{1-e} - e) \tag{2.39}$$

where

$$e = 1 - (\frac{d}{h})^2 [5] \tag{2.40}$$

2.4 Drag

The general equation for drag is

$$F_D = -\frac{1}{2}\rho c_d A_p v_e |v_e| \tag{2.41}$$

Where, c_d, is the drag coefficient, A_p, is the projected area perpendicular to the flow velocity, v_e, at that point.

For the axial drag, this becomes

$$X_{drag} = -\frac{1}{2}\rho c_{da}\pi(\frac{d}{2})^2 u|u| \tag{2.42}$$

where the axial drag coefficient, c_{da}, of a cylinder is 0.2 [13].

For crossflow drag, the flow velocity at each point along the hull, x, is

$$v_e = v + rx \tag{2.43}$$

In Prestero, v_e, was broken up into v and rx components to compute $Y_{v|v|}$, $N_{v|v|}$, $Y_{r|r|}$, and $N_{r|r|}$ [13]. This simplification allows for v and r to be decoupled, so that the values only have to be computed once. However, this simplification is inaccurate, as v and r cannot be

decoupled. Here, the general formula for drag will be used for its accuracy.

$$Y_{drag} = -\frac{1}{2}\rho c_{dc}\int_{x_{b2}}^{x_t} 2R(x)(v+rx)|v+rx|dx \\ -(\frac{1}{2}\rho 2S_{rud}c_{df})(v+rx_{rud})|v+rx_{rud}| \quad (2.44)$$

$$N_{drag} = -\frac{1}{2}\rho c_{dc}\int_{x_{b2}}^{x_t} 2xR(x)(v+rx)|v+rx|dx \\ -x_{rud}(\frac{1}{2}\rho 2S_{rud}c_{df})(v+rx_{rud})|v+rx_{rud}| \quad (2.45)$$

Where, c_{dc}, is the drag coefficient of a cylinder with a value of 1.1 [7], and c_{df}, is crossflow drag coefficient of the rudders, calculated using the rudder fin taper ratio, t.

$$c_{df} = 0.1 + 0.7t \quad (2.46)$$

The control surfaces make up only a minor component of the overall crossflow drag, so for simplicity, only the drag of the rudder will be considered, and the drag of the added fins will be ignored in the calculation. Unlike the simplified form of the drag, equations 2.44 and 2.45 have to be computed every time the velocity changes, and so must be computed at every time step in a simulation, increasing the overall computational complexity.

2.5 Propulsion

It is assumed that at steady state velocity, the propulsion force of the vehicle counters the axial drag force.

$$X_{propulsion} = -X_{uu}u|u| \quad (2.47)$$

2.6 Combining Coefficients

Some of the hydrodynamic coefficients have multiple components, such as Y_{uv}, which has lift from both the body and the control surfaces. All such coefficients, made up of the summation of their parts is as follows

$$Y_{uv} = Y_{uv_b} + Y_{uv_r} + Y_{uv_f} \tag{2.48}$$

$$Y_{ur} = Y_{ur_r} + Y_{ura} + Y_{ur_f} \tag{2.49}$$

$$N_{uv} = N_{uv_b} + N_{uv_r} + N_{uva} + N_{uv_f} \tag{2.50}$$

$$N_{ur} = N_{ur_r} + N_{ura} + N_{ur_f} \tag{2.51}$$

Chapter 3

Metrics of Maneuverability and Stability

In chapter two, the relevant hydrodynamic coefficients for the horizontal plane were derived. These coefficients allow one to understand how the vehicle will behave during maneuvers. In this chapter, the vehicle's behavior will be investigated, in order to hone into a few critical parameters for determining how well a given vehicle will perform, and therefore whether it is a good design choice. In general, all designers are trying to balance between the need to be stable, so as not be effected by small perturbations, in controls or environment, for gathering of data from the environment through sensors, and highly maneuverable, in order to be able to respond rapidly to changes, such as for turning around obstacles. For almost any vehicle mission, there will be a need for each at different times. However, these two parameters are in opposition to each other.

3.1 Stability

One of the most important parameters in vehicle design, for seakeeping, is the stability parameter, C, which determines a vessel's capability of being controlled. This value must always be greater than zero, to be stable, and controllable [14]. If this is not true, the vehicle may instead spin out uncontrollably. However, the larger the value is, the harder it is to maneuver, as the vehicle is more resistant to change. Its takes longer and is more difficult for the vehicle to respond to a change in parameter. For example, it takes longer to make a turn, and said turn has a larger radius. Therefore, it is ideal to achieve a value

that is above the critical point, of zero, for controllability, but also as close to this value as possible, in order to have the most maneuverability. For linear stability, the criterion, C, takes the form.

$$C = -Y_v(mx_GU - N_r) + N_v(mU - Y_r) \tag{3.1}$$

where, x_G is the location of the vehicle's center of gravity. For the REMUS, it will be assumed that the center of gravity occurs at the location of the CoB in this instance. Y_v, Y_r, N_v, and N_r are the same coefficients as, Y_{uv}, Y_{ur}, N_{uv}, and N_{ur}, respectively, derived in chapter two, but multiplied by the forward speed, U, in order to linearize them [14]. In this form, N_v usually plays the stongest role in determining the value of C [14]. However, equation 3.1 can be recast into the form

$$C = -Y_v(mU - Y_r)(x_r - x_{AC}) \tag{3.2}$$

where, x_r, is the Center of Rotational Motion, the location where the Y force acts when a vehicle performs a pure, steady, rotational motion, with forward speed, U (i.e v=0), and, x_{AC}, is the Aerodynamic Center, the location where the Y force acts for a vehicle under pure linear translation (i.e. r=0). The expressions for the Center of Rotational Motion, x_r, and the Aerodynamic Center, x_{AC}, are

$$x_r = \frac{mx_GU - N_r}{mU - Y_r} \tag{3.3}$$

and

$$x_{AC} = \frac{N_v}{Y_v} \tag{3.4}$$

respectively [14]. The form of equation 3.2 allows for easier determination of the critical parameters of this criterion. The hydrodynamic coefficient, $-Y_v$, is always positive, since Y_v is a resistance force to the side velocity, v, and is therefore always negative. The quantity, $(mU - Y_r)$ is also almost always positive, as mU tends to be much larger than Y_r, which means the only quantity that can affect the sign of the stability is $(x_r - x_{AC})$. Knowing this, then the following inequality of equation 3.5 must hold in order for the stability criterion, C, to be positive, and the resulting vehicle controllable.

$$x_r > x_{AC} \tag{3.5}$$

As the stability index, C, becomes more positive, the stability of the vehicle increases. Likewise, equation 3.5 implies that as x_r grows in comparison to x_{AC} (as long as the ratio is above a critical value of 1) the same will be true. Because of this, one should be able to look at the ratio of the two quantities as a metric of quantifying the stability of the vehicle, in place of looking at the stability index as a whole. To validate this observation, the stability coefficient, calculated with equation 3.1 is compared to $\frac{x_r}{x_{AC}}$ through plotting how the values change in fin position, as seen in figures 3-1a and 3-1b respectively. In figure 3-1a, the stability index, C, is always above the original REMUS's value, but reaches a minimum, when the added fin is located 0.1 body lengths (BL) ahead of the CoB. in figure 3-1b on the other hand, the ratio $\frac{x_r}{x_{AC}}$, becomes less than the REMUS's original value when the added fin's location is further forward than 0.11 BL ahead of the CoB, but is still above a critical value of 1 for maintaining stability.

The discrepancy between the two metrics implies that either equation 3.5 cannot be considered a critical quantity, with the other terms in equation 3.2 holding equal weight in determining the stability of the vehicle, or the overall stability criterion used in this system is flawed, and the ratio $\frac{x_r}{x_{AC}}$, is a more critical quantity in determining the maneuverability of the system. In order to determine which assumption is more valid, simulations and experiments must be performed, to determine the stability maneuverability trade-off of the system, which first requires an understanding of maneuverability in underwater systems, and what metrics are used for measurement.

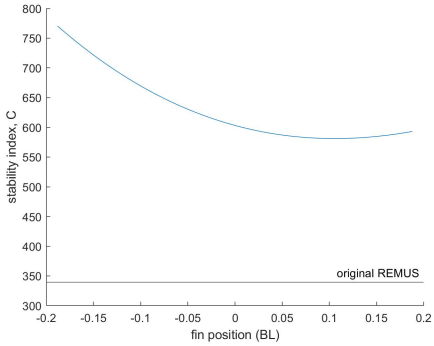

(a) Theoretical stability index, C, of the REMUS as the location of the added fin changes.

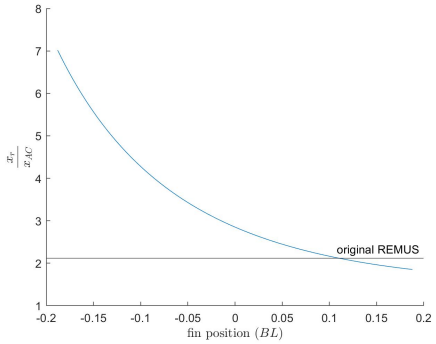

(b) the ratio between the Center of Rotational Motion, x_r, and the Aerodynamic Center, x_{AC}, as the location of the added fin changes.

Figure 3-1: Theoretical stability parameters as a function of added fin position, where the fin position is measured in terms of body lengths (BL) away from the CoB. The horizontal black line is the value for the Original REMUS without added fins.

3.2 Maneuverability

As discussed, knowing that a vehicle is stable, does not mean that it is highly maneuverable, which is desirable for many vehicle mission types. There are several performance metrics commonly used to measure the maneuverability of a vehicle: Dieudonné Spiral, zig-zag maneuver, and the circle maneuver.

In the Dieudonné Spiral, a mission is programmed for a vehicle to follow a growing spiral pattern and then a shrinking spiral in the opposite direction. This is achieved by setting the rudder from 15° to -15° in 5° decrements, waiting for steady state speed and yaw, before each rudder change is made. This test shows whether the vehicle experiences memory effects, observed through a hysteresis in yaw rate, r. If this phenomena occurs, the vehicle will be observed as stuck in a turn and will not respond to change unless strong corrective measures are taken [14].

During the zig-zag maneuver, a steady forward speed is given and achieved, after which the rudder is given deflection commands of alternating ± 20°. Between each change, the command is held, until the vessel turns to the commanded degree. From this maneuver, the response time to reach its heading, the yaw overshoot above the commanded heading, and the period between the ± 20° oscillations are all measured. In general, this maneuver tests

the vehicle's responsiveness to changes in commands [14].

The last common maneuver is the circle maneuver, in which after steady forward speed is achieved, the vehicle is given a rudder command that causes the vehicle to turn in a circle. After steady turning is achieved, one can measure the turning radius, the loss of speed from the commanded forward speed, and the drift angle, β. The drift angle is related to the speed loss and an important metric for maneuverability as it measures how much sideslip occurs, seen through side velocity, v, as the vehicle makes a circle, expressed in through the equation

$$v = -Usin(\beta) \tag{3.6}$$

The vehicle slipping during the turn means energy is being wasted. As the drift angle increases, the profile of the vehicle perpendicular to the circle and direction of motion increases, increasing the drag on the vehicle, and slowing it down. When battery life is already limited in underwater vehicles, one wants to limit excess energy loss. The turning radius also indicates how small of a circle the vehicle can make [14].

All of the maneuverability tests give information on how well a vehicle a maneuvers, by how fast the vehicle responds, and how tight of a turn it can achieve. Having the best performance of these metrics is critical for a vehicle that must navigate obstacle-infested environments. For the scope of this work the circle maneuver is the focus, as it is the easiest to extract measurements in an experimental setting and is still quite telling of the vehicle's behavior.

3.3 Simulation

The stability metrics, described in section 3.1, focus on steady state response, and as mentioned, need simulation to determine whether the overall stability index, of equation 3.1, or the criteria, of equation 3.5, is more critical for indicating the maneuverability of a vehicle. Using nonlinear simulations, modeling of the circle maneuver described in section 3.2 are investigated. All of the relevant hydrodynamic coefficients derived in chapter two, are used to formulate the external forces acting on the vehicle, described in equations 3.7 through 3.9, while the dynamics of the system are given in equations 3.10 through 3.12.

$$X_{ext} = X_{u|u|}u|u| + X_{\dot{u}}\dot{u} + X_{vr}vr + X_{rr}rr + X_{prop} \tag{3.7}$$

$$Y_{ext} = Y_{\dot{v}}\dot{v} + Y_{\dot{r}}\dot{r} + Y_{ur}ur + Y_{uv}uv + Y_{uu\delta_r}u^2\delta_r + Y_{drag} \tag{3.8}$$

$$N_{ext} = N_{\dot{v}}\dot{v} + N_{\dot{r}}\dot{r} + N_{ur}ur + N_{uv}uv + N_{uu\delta_r}u^2\delta_r + N_{drag} \tag{3.9}$$

$$X = m[\dot{u} - vr - x_G r^2] \tag{3.10}$$

$$Y = m[\dot{v} + ur + x_G\dot{r}] \tag{3.11}$$

$$N = I_z\dot{r} + m[x_G(\dot{v} + ur)] \tag{3.12}$$

The forces and dynamics of these equations can be combined and rearanged into matrix form, where the acceleration terms are kept as the independent variable, as follows

$$\begin{bmatrix} m - X_{\dot{u}} & 0 & -m \\ 0 & m - Y_{\dot{v}} & mx_G - Y_{\dot{r}} \\ -my_G & mx_G - N_{\dot{v}} & I_z - N_{\dot{r}} \end{bmatrix} \begin{bmatrix} \dot{u} \\ \dot{v} \\ \dot{r} \end{bmatrix}$$
$$= \begin{bmatrix} X_{u|u|}u|u| + (X_{vr} + m)vr + (X_{rr} + mx_G)rr + X_{prop} \\ (Y_{ur} - m)ur + Y_{uv}uv + Y_{uu\delta_r}u^2\delta_r + Y_{drag} \\ (N_{ur} - mx_G)ur + N_{uv}uv + N_{uu\delta_r}u^2\delta_r + N_{drag} \end{bmatrix} \tag{3.13}$$

Equation 3.13 is then used to perform the simulation in Matlab, where Runga Kutta Fourth Order method is used to solve for the REMUS behavior, in full, for every time step. However, it is worth noting how this transforms during steady state behavior, to observe how the stability metrics directly factor in. Once steady state behavior is reached after an input of rudder angle, δ_r, the acceleration terms of 3.13 fall out, leaving

$$-Y_v v + (mu - Y_r)r = u^2 Y_\delta \delta \tag{3.14}$$

$$-N_v v + (mx_G u - N_r)r = u^2 N_\delta \delta \tag{3.15}$$

where Y_δ and N_δ are the same as $Y_{u^2\delta}$ and $N_{u^2\delta}$ of chapter two, multiplied by u^2. Combining equations 3.11 and 3.12,and recalling the equation for the stability index, one can solve out for the yaw rate, r,

$$r = \frac{Y_\delta \delta}{C}(N_v Y_\delta - Y_v N_\delta) \tag{3.16}$$

which shows, the relation between yaw rate, and the stability index, C. As the stability of the vehicle increases, the vehicle will be slower to turn, and thus less maneuverable.

Returning back to the simulation, to validate the simulation, experimental data on the REMUS obtained by Prestero was used. In sea trials, of the REMUS executing a circle maneuver from the rudder set to 4° and given nominal speed, U, of 1.5 m/s, the yaw rate of the vehicle was just below 10 $^\circ/s$ and his simulation had the REMUS turning with a radius of about 8 m [13]. These experimental results match the results from the simulation described here, as seen in the black curves in figures 3-4 and 3-2a respectively.

With the original unmodified vehicle simulation verified, the fins could be added to the vehicle at different locations and the same mission executed. While the rudder was set to 4°, the added fina were held at 0°. The resulting turning radii are shown in figure 3-2a, where the horizontal line is the value of the original, unmodified REMUS. For fins located further aft than 0.07 BL in front of the CoB the turning radius is larger than the original vehicle, implying the vehicle is more stable and less maneuverable. It is not until the fins are positioned ahead of 0.07 BL that the turning radius gets smaller than the original REMUS's performance. This improvement continues as the fins shift forward. However, the effect is starting to taper out once the most forward fin position has been achieved, implying there is a limitation to how much improvement can be made to the performance from the addition of added fins.

These results of improved maneuverability corroborate with the ratio $\frac{x_r}{x_{AC}}$ of figure 3-1b rather than stability index, C, of figure 3-1a. This implies that the overall stability metric, C, is not always a good indication of stability. For added fins on REMUS UUV under investigation here, the ratio $\frac{x_r}{x_{AC}}$ is a stronger indicator of the maneuverability. The fin positions, at which turning behavior is improved, in the simulation follows similar to that which was observed looking at $\frac{x_r}{x_{AC}}$ in figure 3-1b, with similar tapering behavior. However, the fin position crossover point for increased performance of turning happened

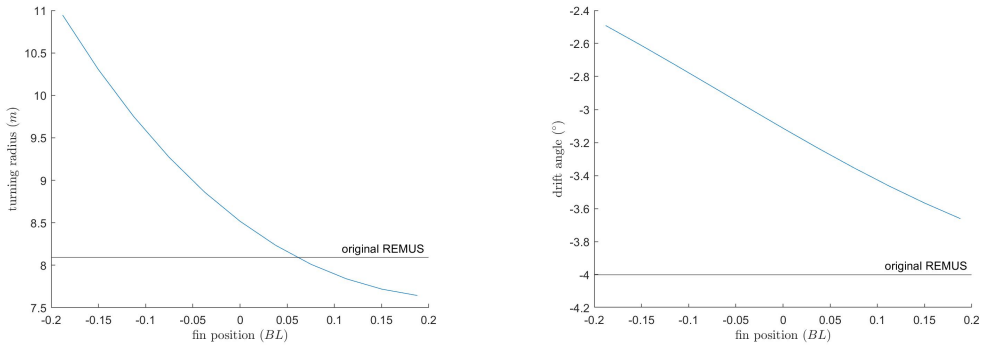

(a) Steady turning radius of the REMUS

(b) Steady drift angle of the REMUS

Figure 3-2: Theoretical steady turning radius and drift angle of the REMUS with a pair of added fins placed at different locations of the hull (blue curves), when given a 4° rudder command and 0° fin command. The horizontal black lines indicate the baseline values of the original, unmodified REMUS

earlier along the hull in the simulation than when observing $\frac{x_r}{x_{AC}}$ directly. In the simulation, the crossover occurred at 0.07 BL as opposed to 0.11 BL. This could occur, because of nonlinear hydrodynamic coefficients that were used in the simulation, but were neglected from the $\frac{x_r}{x_{AC}}$ calculations. For example, quadratic drag is neglected when computing the ratio. Drag in a small quantity helps to push the vehicle into a turn.

From observing the drift angle in figure 3-2b, where the horizontal line is the value of the original, unmodified REMUS, no matter the location of the added fins, the drift angle is smaller in magnitude than that of the original vehicle. However, as the fins move forward along the hull from the rudder, the drift angle magnitude increases linearly. As with the turning radius, when the fin is further to the back, the vehicle is more stable, and so the vehicle will not drift as much as it makes the turn, but it will still take more distance to turn as was observed in figure 3-2a. As the relationship of drift angle to fin position is linear over this range, there is no tapering of the angle as was seen for turning radius, implying that there is a point where the turning radius stops improving, but the drift angle continues to enlarge. At this point, there will be increased drag added to the vehicle, with no added benefit to the vehicle performance. However, in the spot where the fins the are ahead of 0.07 BL in front of the CoB and less than 0.2 BL, the performance in turning is improved while also seeing a decrease in the drift angle, in comparison to the original vehicle.

Moving to the time response, the decrease in drift angle observed, and therefore less drag on the vehicle, will lead to a mild forward speed boost to the vehicle in the case of fins

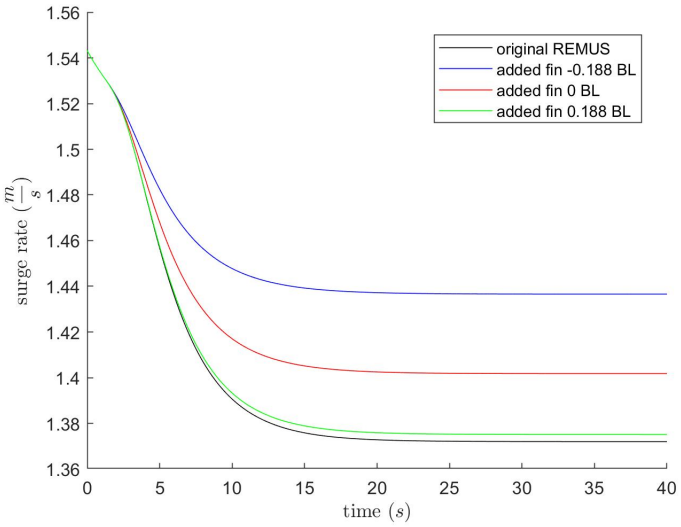

Figure 3-3: Surge velocity of the REMUS during the course of a turn maneuver when given a 4° rudder command and 0° fin command for select fin cases. Depicted are the original REMUS configuration (black), and fins at furthest aft positon (blue), middle position (red), and furthers forward (green)

located at 0.188 BL, as seen in figure 3-3 in comparison to the original REMUS. Only a few other fin positions are depicted for clarity. For the cases with the fin further back on the vehicle, the forward speed is larger than the original REMUS as well, since the vehicle has less drift, but as was seen the turning radii were larger as well. Looking at the yaw velocity response on the other hand, in figure 3-4, only the yaw rate response for the fins at 0.188 BL ahead of the CoB is faster than the original REMUS, which coincides with a smaller turning radius in this configuration.

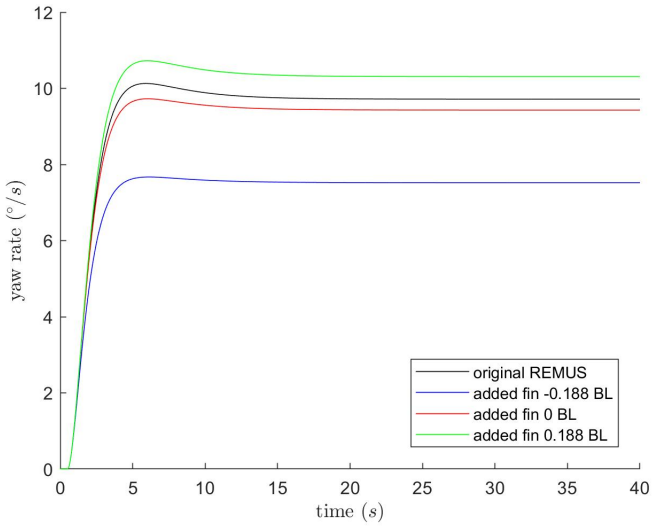

Figure 3-4: Yaw velocity of the REMUS during the course of a turn maneuver when given a 4° rudder command and 0° fin command for select fin cases. Depicted are the original REMUS configuration (black), and fins at furthest aft positon (blue), middle position (red), and furthers forward (green)

Chapter 4

Experimental Validation

To confirm the results of chapter three, physical experiments were performed to measure the necessary hydrodynamic coefficients to determine stability and maneuverability, as the coefficients derived in chapter two are only approximations.

4.0.1 Description of Experimental Model

A half-scale REMUS model was fabricated with a 3D-printed PLA nose and tail and a PVC tube body. The tail included rudders, fixed to the body at 0°. The model had length, L, of 0.67 m, and maximum hull diameter, D, of 0.095 m. An image of the completed model is depicted in figure 4-2. The model had mass, m, of 5.14 kg when filled with water, as occurred during experiments. The model was filled with water during experiments, because complete water proofing would be difficult to obtain, which means as water leaked into the model, the mass of the vehicle and the results of the data would change. Filling the model with water avoided this issue.

The model was attached to all of the experimental setups, via a rod, through the CoB of the full scale UUV, in order to directly compare the experimental results with simulation results. The rod had a mass, m_r, of 0.15 kg, and was attached 0.335 m from the stern of the model. With respect to the rod's location, the center of gravity, x_G, of the model was -0.06 m, and moment of inertia, I_{zz}, was 0.12 kgm^2. Through this rod, a six-degree force-moment sensor was attached for measuring all of the experimental data. This data collection occurred at 1000 Hz.

The actual, robotic REMUS operates at sea at 1.5 m/s, which means in order to maintain

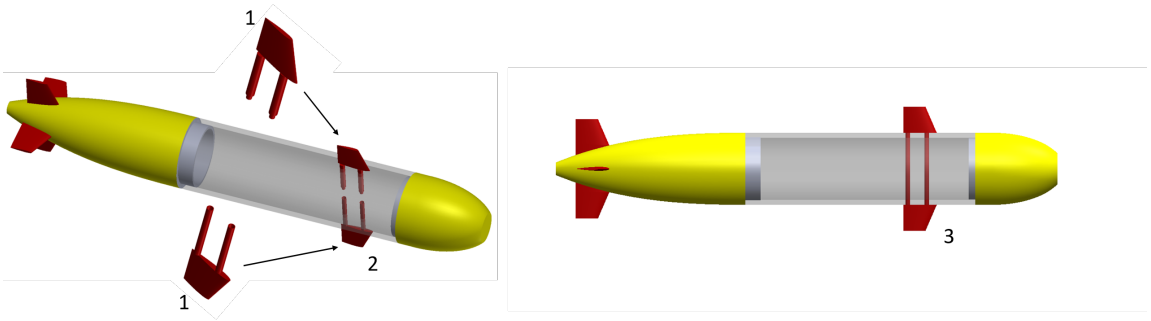

Figure 4-1: CAD model of the experimental model assembly. A pair of added fins with female and male dowel pin connectors (1) fit into equally spaced slots on the model body (2). The fins connect together to then fit snuggly on the model (3).

Reynolds similitude at, 2.88 x 10^5, the model would have to be towed at double this speed, which is not possible in MIT's towing tanks. The Reynolds number is also very close to the critical point between laminar and turbulent flow, which occurs at 3 x 10^5 theoretically [9]. Given, that turbulent flow can be tripped earlier due to hull imperfections and screws on the hull, it is assumed that turbulence has been tripped in the full scale vehicle. Because of this, all surfaces on the model were roughened up, in order to help trip turbulent flow during experiments. Even though it is not possible to maintain exact Reynolds similitude, it is important to maintain the same regime between experiments. To prevent surface effects during testing, the model was fixed at least two diameter lengths below the surface of the water during experiments.

In order to test the effect of added fins on the model, holes were drilled along the body of the model, in 0.025 m increments. A 3D-printed PLA added fin, on a pair of dowel pins could be slotted into two sequential holes, and then connected to another fin on the other side. This assembly process is depicted in figure 4-1. The fins were secured to the dowel pins so that their center of action aligned halfway between the dowel pins.

The hole placement allowed for fins to be added anywhere between 0.17 body lengths in front of the CoB, and -0.14 body lengths behind. This range was chosen, because the effect of added fins was only investigated on the section of the body where the diameter was constant. The effect of fins on the nose and the tail were not investigated, as this would require a more complex experimental design to fix the fins to a sloping hull. The full range of the possible fin positions are shown on the CAD models in figure 4-3. An example of the physical experimental model with a set of forward added fins are depicted alongside the

original REMUS in figure 4-2.

When the holes for the fins were not in use, they were plugged up with rubber stoppers, so as not to affect the flow of water over the body. The holes on the model can be clearly seen along the top of the hull in figure 4-2.

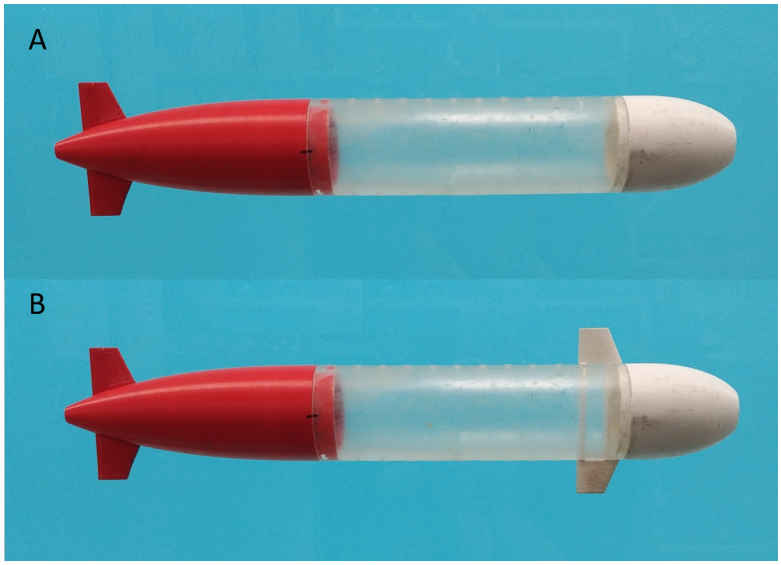

Figure 4-2: The manufactured experimental model. A) the original configuation of the model, B) the model with fins added at 0.17 body lengths (BL) in front of center of buoyancy (CoB)

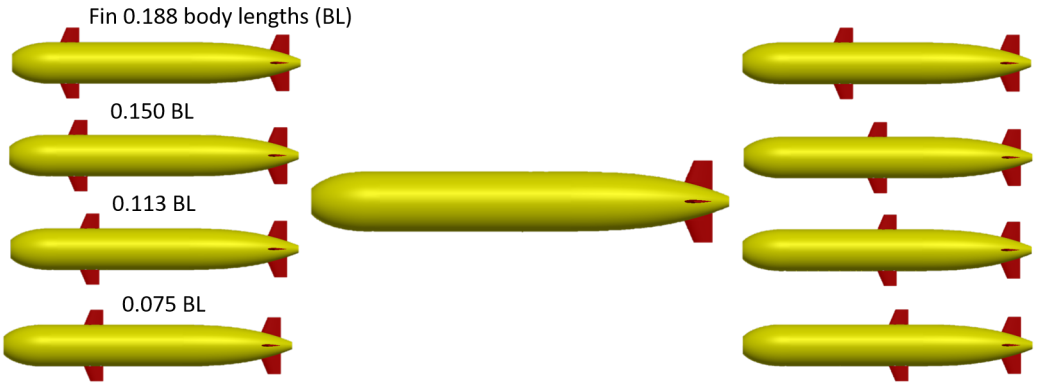

Figure 4-3: CAD renderings of the model, where the central figure is the original configuration of the model. Surrounding this model are the model with the different fin positions possible, measured with respect to the center of bouyancy of the model (CoB) in terms of model body length (BL)

4.0.2 Static Experiments

Initial experiments were performed in the MIT towing tank, which measures 100ft x 8ft x 4ft. The model was towed statically down the tank with a speed, U, of 0.4 m/s, and at an angle of attack, θ, with respect to the towing direction. This speed was chosen, as it minimized unwanted vibrations of the model. The angle of attack was varied between -30° and 30°. From -5° and 5°, experiments were performed in 1° increments. Experiments beyond these bounds were performed in 5° increments. The angle of attack of the model, in the body's coordinate frame, is indicated in figure 4-4b. Static towing at an angle, is equivalent to the vehicle being toward with a forward velocity, u, and a side velocity, v, of values

$$u = Ucos\theta \tag{4.1}$$

$$v = -Usin\theta \tag{4.2}$$

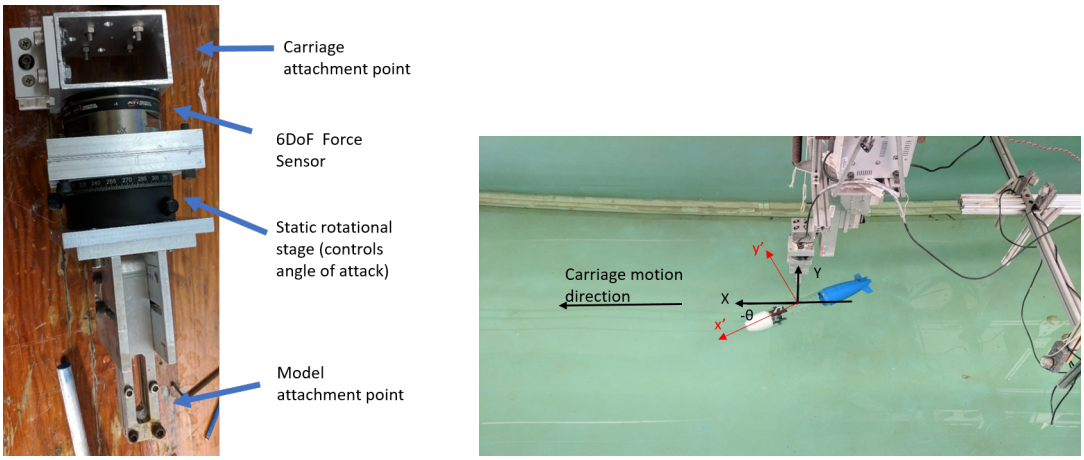

(a) The mount for static experiments. A rotational stage placed between the force sensor and the attachment point of the model causes a coordinate change between the sensor and the model

(b) The model setup in the MIT towing tank. Direction of cariage motion indicated, as well as the coordinate frames. The global coordinate frame of the sensor is in black, and the model coordinate frame is in red

Figure 4-4: Static experimental setup

The rotational stage for positioning the angle of attack, θ, was positioned between the model and force sensor, as indicated in figure 4-4a. Because of this, a coordinate transformation was required to change the sensor data from the global reference frame of the towing

carriage (the black coordinate system in figure 4-4b) to the model reference frame (the red coordinate system in 4-4b). The coordinate transformation from the global reference frame to the model reference frame is as follows:

$$x' = Xcos\theta + Ysin\theta \tag{4.3}$$

$$y' = Ycos\theta - Xsin\theta \tag{4.4}$$

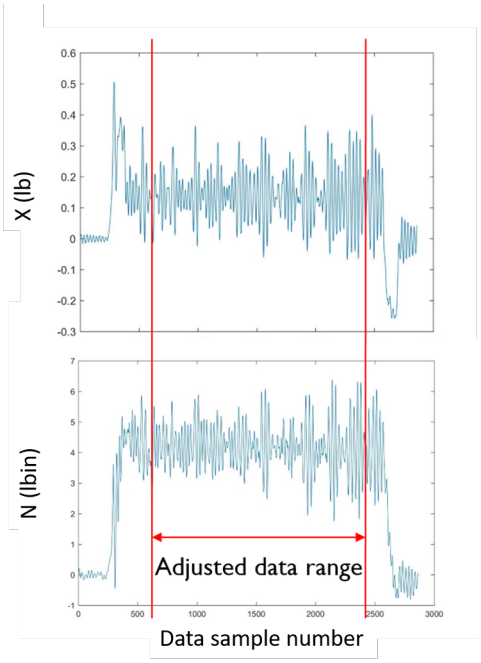

Figure 4-5: Raw data collected from the sensor. The data in between the vertical lines occurs during steady state is conditions, and is kept for processing. The rest is discarded, as acceleration effects are present

Once the data was transformed into the model reference frame, a relationship between the Y force and N moment, and the side velocity, v, could be determined. During processing of the data, the data during the acceleration and deceleration of the carriage was cut out, an example of which is depicted in figure 4-5, leaving only the steady state response for analysis. The remaining data was averaged to obtain the force measurements for each trial. Three trials were performed for each experimental permutation and used to find the best fit curve for each fin position.

The force, Y, was fit to

$$Y = av|v| + bv \tag{4.5}$$

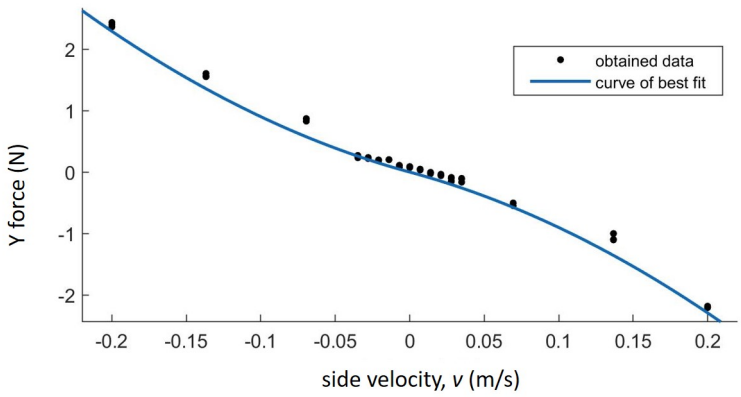

Figure 4-6: Fitting the obtained Y data (the dots) for the original REMUS to a curve of best fit (blue line)

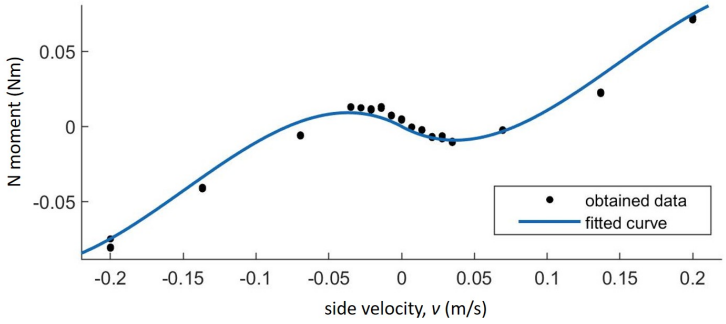

Figure 4-7: Fitting the obtained, N, data (the dots) for the original REMUS to a curve of best fit (blue line)

and the horizontal moment, N, was fit to

$$N = av^3 + bv|v| + cv \tag{4.6}$$

Where a, b, and c are the coefficients to be determined. Equations 4.5 and 4.6 are of this form, because Y and N will inevitably include drag, as drag cannot be eliminated during experiments. Drag terms as were derived in chapter two, once integrated, take the form of these equations, and as the highest order expression, play a dominant role in determining the shape of the curve. These functions were a good fit for the data, as when fitted to the data for the original REMUS, the curve has a R-squared value of 0.9797 for Y and 0.9695 for N, visualized in figures 4-6 and 4-7.

All of the fitted curves for the data are plotted in Figures 4-8 and 4-9 for Y and N respectively. The coefficients for the curves are listed in the appendix, in tables A.2 and A.3.

Figure 4-8 shows there is very little variation in Y between the different fin positions, as all the plots are very closely clustered together, with all the fin positions having a higher local slope around the origin, than the original REMUS. This was expected, because from chapter two, it is understood that Y has no relation on the fin placement. Y only depends on the fin area and aspect ratio. Therefore, adding an extra fin increases Y, but it is not expected for there to be a variation based off of fin position. N on the other hand depends strongly on the fin position. As the fin position shifts further forward along the hull, the local slope of the curve, near the origin, becomes sharper, (i.e. N increases), but is not until the added fin is at least -0.075 BL from the CoB that the N surpasses the original REMUS. N is a critical coefficient, as an increase in N increases x_{AC}, which decreases the ratio $\frac{x_r}{x_{AC}}$ and improves the maneuverability. From this result, having the fin as far forward as possible appears to be desirable for maneuverability.

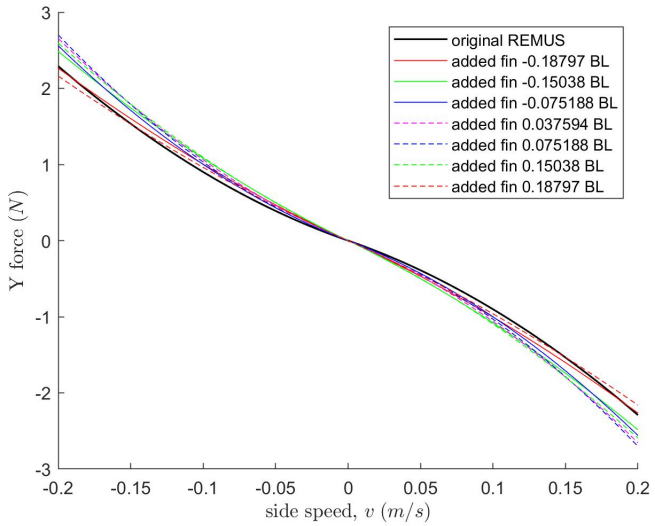

Figure 4-8: The fitted Y curves as a function of the side velocity, v, for each posible fin position. The thicker black curve is the original REMUS, the solid colored lines are for added fins behind the CoB, and the dashed colored lines are for added fins ahead of the CoB

Since this experiment expanded into the nonlinear range of the coefficient's behavior, it allows for observations not taken into account in the coefficient derivations. The maximum value of N increases with fin position, and more importantly, the magnitude of the speed or related angle of attack, at which this peak occurs increases as well. This peak in moment marks where stall begins to occur, which for underwater vehicles is the point where vehicles can get stuck in turns, and are either impossible to bring back on course, or require a large

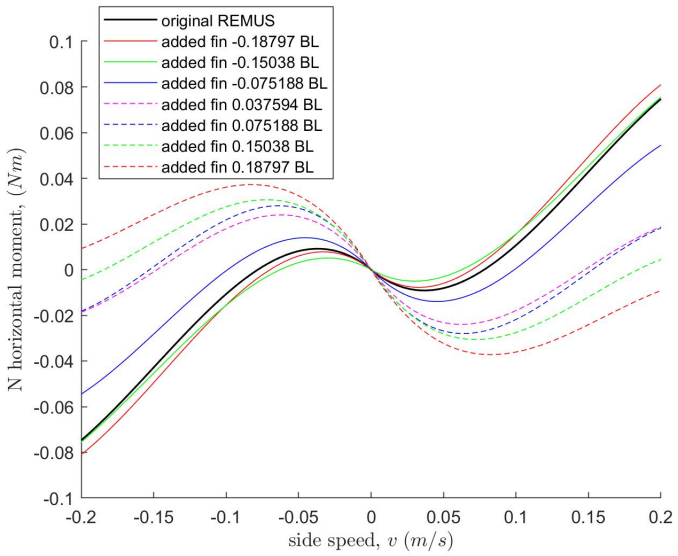

Figure 4-9: The fitted N curves as a function of the side velocity, v, for each posible fin position. The thicker black curve is the original REMUS, the solid colored lines are for added fins behind the CoB, and the dashed colored lines are for added fins ahead of the CoB

over correction. Having a larger range of speeds or angles before stall occurs makes a vehicle easier to control, as well as able to execute sharper turns, before having to be concerned about stall. Stall is also a nonlinear response, and so delaying it allows one to expand the range for which linear approximations may hold. Having the fins as far forward as possible allows for the best anti-stall behavior.

4.0.3 Dynamic Experiments

The above experiments were for a towed model, under static conditions. However, the real vehicle is propelled under its own power. The previous experiments also could not look at the angular velocity of the vehicle. In order to perform more realistic experiments, and determine the relationship of the Y force and N moment to sway velocity, v, and yaw angular velocity, r, dynamic experiments were performed at the MIT Sea Grant Intelligent Towing Tank, depicted in figure 4-10. This towing tank measures 1m x 1m x 10m, and has a 4 DoF towing carriage, with control in the x, y, and θ axes, where the x axis motion is controlled through two motors. One of the x axis motors controls the overall steady motion, and a second motor controls the unsteady, added motion. For these experiments, motions were programmed so that the vehicle felt the forces of a self-propelled vehicle, instead of a towed one. To achieve this, the model coordinate frame's forward motion must remain constant.

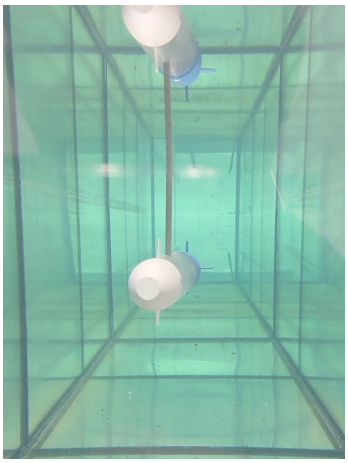

(a) front view

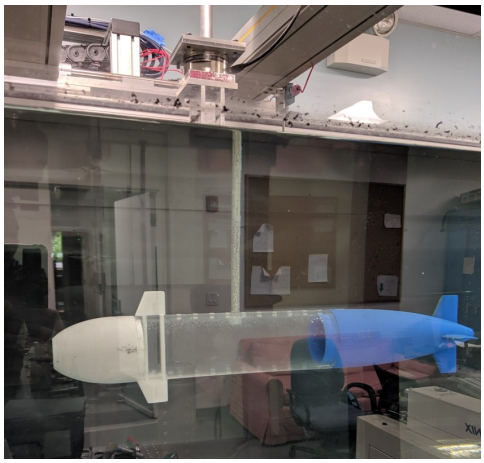

(b) side view

Figure 4-10: Model experiments in the Sea Grant towing tank. The force sensor is connected directly between model and the carriage motors

The general forms of the velocities controlling the towing carriage are the following:

The forward, surge speed was programmed as

$$u = Ucos(\theta) \tag{4.7}$$

and side, sway speed as

$$v = -Usin(\theta) + v_1(t) \tag{4.8}$$

Lastly the angular, yaw velocity, was programmed as

$$r(t) = \frac{d\theta}{dt} \tag{4.9}$$

where, θ, is the yaw angle of the model, and, U, was set to 0.25 m/s.

Yaw and sway behavior of the model were investigated separately, requiring specific variations of the above equaitons. For imposed sway experiments the specific programmed behavior was

$$\begin{aligned} v_1(t) &= 0.1Usin(2\pi ft) \\ \theta(t) &= 0. \end{aligned} \tag{4.10}$$

Where, the frequency, f, was varied from 0.1 to 0.25 Hz, and the magnitude of v_1 was

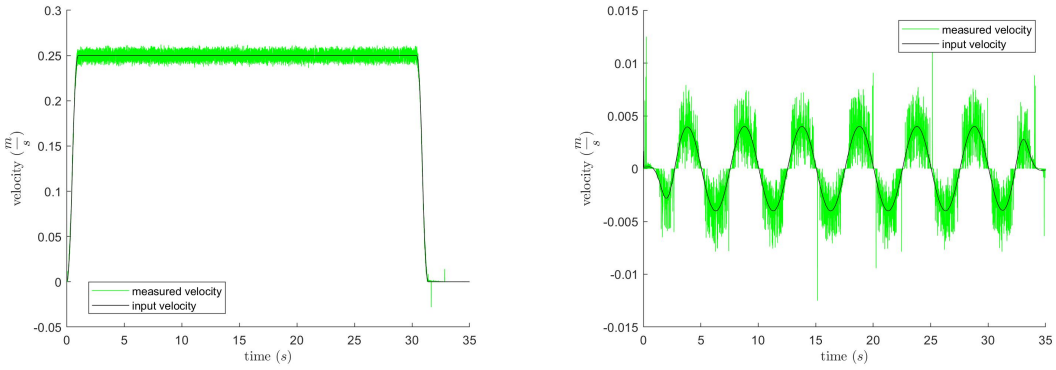

(a) forward velocity, U (b) the side velocity, $v(t)$

Figure 4-11: Programmed and measured velocities of the model during sway experiments

10% of U. Examples of the imposed speeds as well as the measured values are exhibitied in figures 4-11a and 4-11b.

For imposed yaw motion experiments, the programmed behavior was:

$$\theta(t) = \theta_0 sin(2\pi f t) \tag{4.11}$$

$$v_1(t) = 0 \tag{4.12}$$

Where the magnitude of the yaw, θ_0, was set to 5°, and the frequency was varied from 0.3 to 0.5 Hz. Figures 4-12a and 4-12b depict the varying input velocities and their measured values. For the forward velocity, the main x-axis motor moved with a constant speed, very similar to as seen in figure 4-11a, while the small xx-axis motion was superimposed to create the variability in speed and is the speed profile depicted in figure 4-12a.

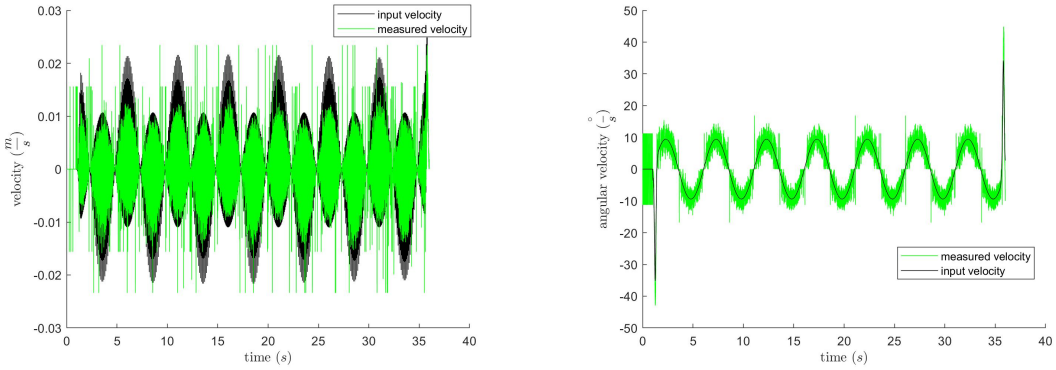

(a) small xx-axis forward velocity, $\dot{xx}(t)$ (b) yaw velocity, $\dot{\theta(t)}$

Figure 4-12: Programmed and measured velocities of the model during yaw experiments

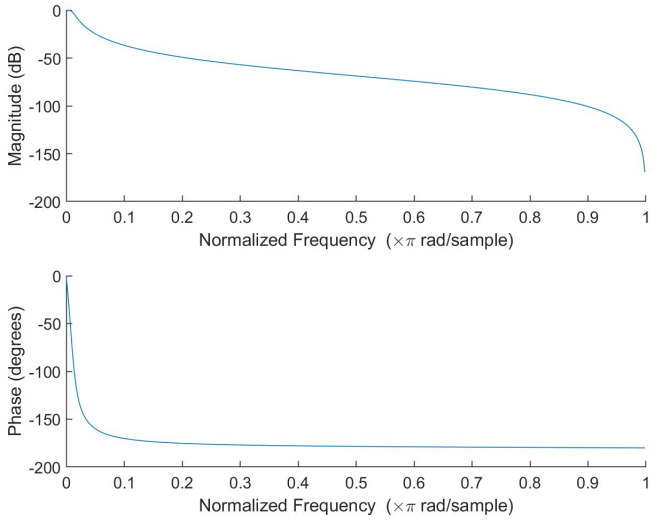

Figure 4-13: single iteration of the lowpass filter used to filter the data

Position, velocity, and force data were collected, all in the frame of reference of the model, as the sensor was attached between the model and the motors of the carriage. The force data was compressed in order to have the same frequency of data collection as the motion data. During signal processing, the data was then passed through a low pass filter to remove the effects of the carriages control. The Sea Grant tank already has PID control for position and velocity control, to minimize adding vibrations to the system during tests. However, these experiments were at the edge of the capability of the tank, and so a strong low pass filter, to only keep frequencies in the range being tested, was designed. The data was sampled at 1000 Hz and the filter was designed to have 3 dB of ripple in a 0 to 6 Hz passband, and 6 dB of attenuation in the stopband at 8 Hz, by using the Matlab buttord command. A single pass of the filter is depicted in figure 4-13. All velocity data was passed once through this filter, while the force and moment data was filtered twice. An example of the resulting Y force and N moment data, when passed through the filter twice, is exhibited in figures 4-14a and 4-14b respectively.

Once filtered, and the data during the initial acceleration and final decceleration of the carriage have been removed, the remaining data was fit to a sum of sines function of the form,

$$f(t) = Asin(\omega t + \phi) \tag{4.13}$$

Where, $f(t)$ is the data to be fitted: the Y force, N moment, the sway velocity, v, or the yaw

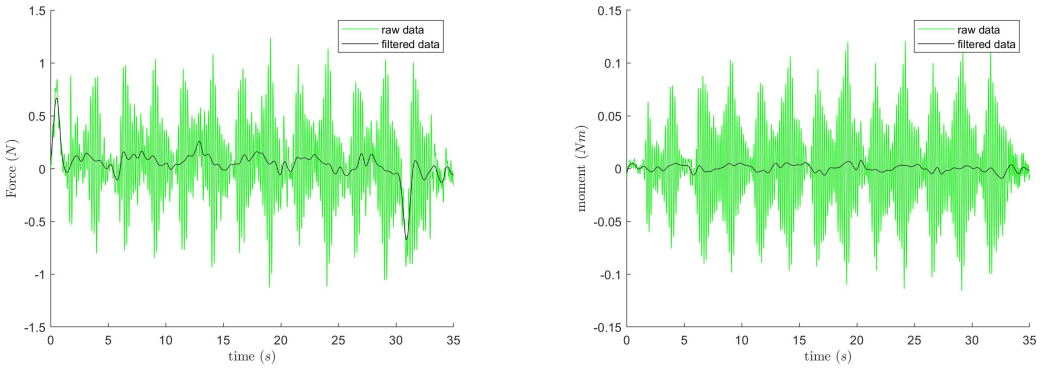

(a) example Y force (b) example N moment

Figure 4-14: example of raw and filtered data collected during dynamic model experiments

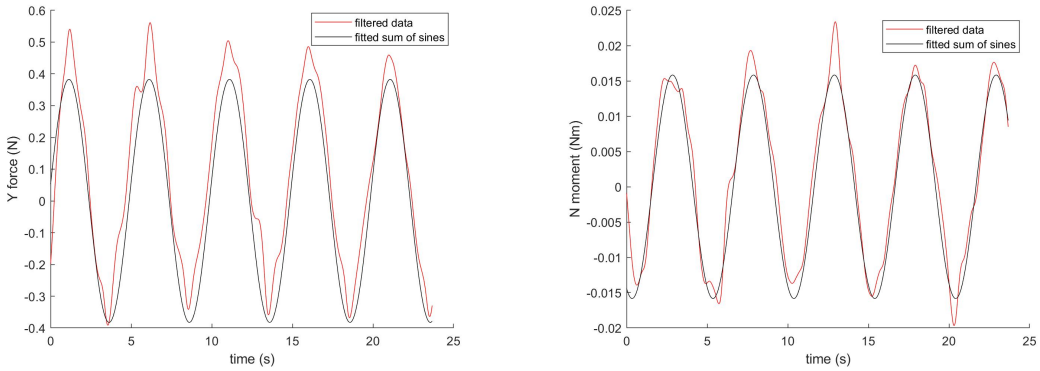

(a) Example fitted Y force (b) Example fitted N moment

Figure 4-15: Fitting filtered Y force and N moment data from dynamic experiments to a sum of sines

angular velocity, r. A, is the amplitude of the sin wave, ω, is the frequency of oscillation, and ϕ, is the phase shift of the sine curves. The velocities are the real, measured values, rather than the programmed values, for error reduction. A sum of sines function was chosen as the curve fit type, because, since water has memory effects, there will be a slight phase delay, ϕ between the velocity of the model and the forces the model feels in reaction, and so it is not expected for the force to be a simple sine function, like the input. Examples of the fitted forces are depicted in figure 4-15a and 4-15b.

Acceleration data was not measured directly, but was determined through taking the difference between sequential velocity points and dividing by the time between samples. The first value was determined, through interpolation, to avoid an infinite acceleration between time t=0 and the first measured value.

With the fitted data, and assuming linearity, the measured forces should be of the form

$$(m - Y_{\dot{v}})\dot{v} - Y_v v + (mU - Y_r)r + (mx_G - Y_{\dot{r}})\dot{r} = Y \tag{4.14}$$
$$(I_{zz} - N_{\dot{r}})\dot{r} - N_v v + (mx_G U - N_r)r + (mx_G - N_{\dot{v}})\dot{v} = N \text{ [14]}$$

which could be used to calculate the hydrodynamic coefficients. For experiments on the model experiencing sinusoidal sway velocity, the yaw velocity and acceleration terms drop out in equation 4.14. Integrating over the time, the remaining components, the sway coefficients can be computed as:

$$Y_v = -\frac{\int Y(t)v(t)dt}{\int v(t)^2 dt} \tag{4.15}$$

$$N_v = -\frac{\int N(t)v(t)dt}{\int v(t)^2 dt} \tag{4.16}$$

$$Y_{\dot{v}} = m - \frac{\int Y(t)\dot{v}(t)dt}{\int \dot{v}(t)^2 dt} \tag{4.17}$$

$$N_{\dot{v}} = mx_G - \frac{\int N(t)\dot{v}(t)dt}{\int \dot{v}(t)^2 dt} \tag{4.18}$$

For the experiments of the model experiencing sinusoidal yaw velocity, the sway related terms of equation 4.14 drop out. Integrating over time, the remaining components, the yaw coefficients are computed as:

$$Y_r = mU - \frac{\int Y(t)r(t)dt}{\int r(t)^2 dt} \tag{4.19}$$

$$N_r = mx_G U - \frac{\int N(t)r(t)dt}{\int r(t)^2 dt} \tag{4.20}$$

$$Y_{\dot{r}} = mx_G - \frac{\int Y(t)\dot{r}(t)dt}{\int \dot{r}(t)^2 dt} \tag{4.21}$$

$$N_{\dot{r}} = I_{zz} - \frac{\int N(t)\dot{r}(t)dt}{\int \dot{r}(t)^2 dt} \tag{4.22}$$

Table 4.1: Sway hydrodynamic coefficients

Fin position [body length]	Y_v $[kg/s]$	N_v $[kgm/s]$	$Y_{\dot{v}}$ $[kg]$	$N_{\dot{v}}$ $[kgm]$
original REMUS	-2.969	-0.176	-5.621	0.068
-0.150	-5.178	-0.072	-5.779	0.174
-0.113	-5.194	-0.127	-5.788	0.180
-0.075	-5.303	-0.134	-5.645	0.168
0.038	-5.315	-0.234	-5.360	0.170
0.075	-5.332	-0.256	-5.834	0.135
0.113	-5.401	-0.301	-5.620	0.129
0.150	-5.682	-0.344	-5.474	0.141
0.188	-5.726	-0.401	-5.520	0.143

Table 4.2: Yaw hydrodynamic coefficients

Fin position [body length]	Y_r $[kgm/s]$	N_r $[kgm^2/s]$	$Y_{\dot{r}}$ $[kgm]$	$N_{\dot{r}}$ $[kgm^2]$
original REMUS	1.001	-0.217	0.212	-0.022
-0.150	1.242	-0.237	0.130	-0.026
-0.113	1.200	-0.229	0.129	-0.024
-0.075	1.111	-0.227	0.190	-0.023
0.038	0.996	-0.215	0.185	-0.023
0.075	0.973	-0.219	0.178	-0.024
0.113	0.994	-0.221	0.144	-0.024
0.150	0.912	-0.226	0.180	-0.024
0.188	0.798	-0.233	0.202	-0.023

The resulting sway and yaw coefficients are listed in tables 4.1 and 4.2 respectively. To more clearly observe how the coefficients are affected by the added fins, a ratio between the coefficient value at each fin position and the original REMUS's value was obtained and

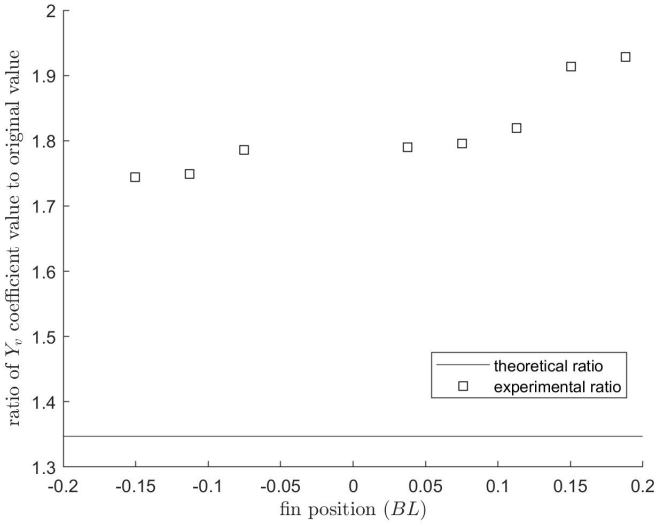

(a) Y_v

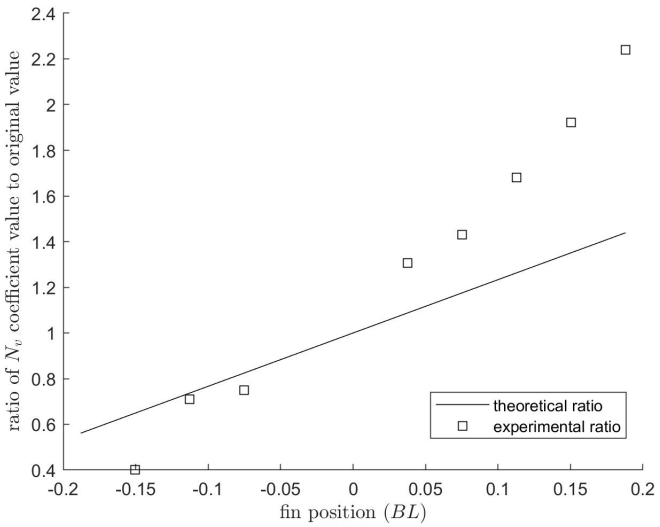

(b) N_v

Figure 4-16: The ratio of the hydrodynamic coefficient, related to sway velocity, v, at each fin position, compared to the original REMUS value, both experimentally and theoretically

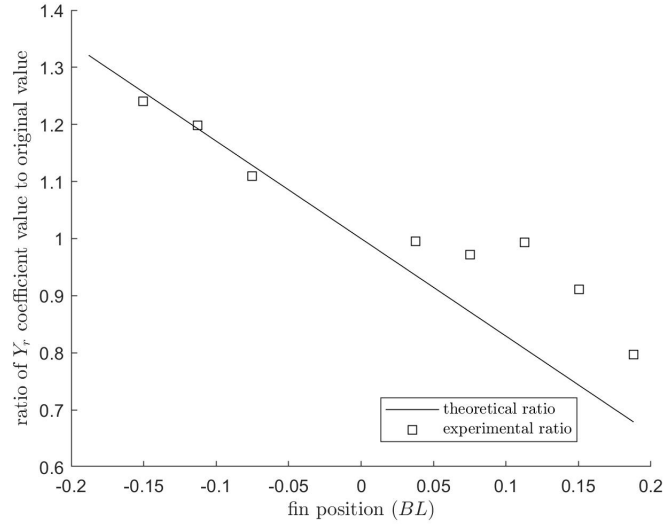

(a) Y_r

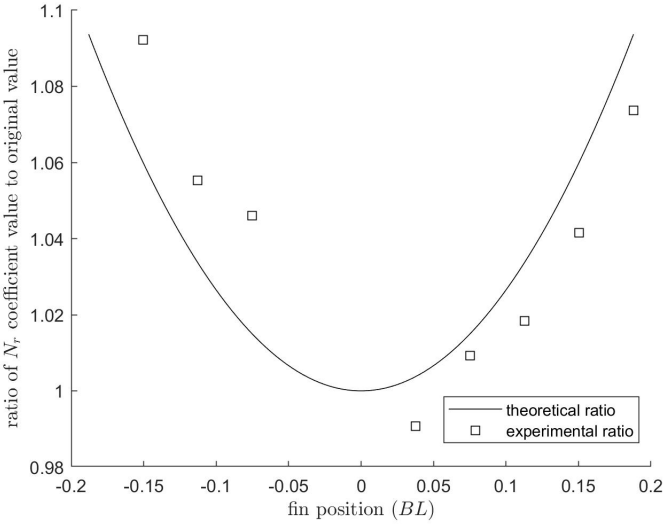

(b) N_r

Figure 4-17: The ratio of the hydrodynamic coefficient, related to yaw velocity, r, at each fin position, compared to the original REMUS value, both experimentally and theoretically

plotted. For Y_v, N_v, Y_r, and N_r, the experimental ratios are compared to the expected theoretical values in figures 4-16a through 4-17b. Experimentally, the fins had a stronger effect on Y_v than was expected, as seen in figure 4-16a. Adding fins lead to an approximate 1.8x increase in Y_v, when only a 1.35x increase was expected. This potentially occurred because, in theoretical calculations, the REMUS was self-supported, but in experiments, a rod was needed for attachment, and so the force sensor was measuring the force against the rod, in addition to the model. Additionally, the ratio should have been constant, but as the fins shifted forward on the body, the ratio increased mildly. N_v in figure 4-16b also exhibited a stronger effect with fin position than expected, with N_v increasing, more sharply with a forward moving fin position, than theory predicts. Lifting theory assumes potential flow over the body, with the fluid closely following the body [14]. Near the back of the body where the flow has fully developed, this assumption is valid. However, as the fin shifts closer towards the front of the body, the flow of water may not have fully developed, which could lead to a nonlinearity in the force development. This is an interesting and important observation, considering N_v is assumed to play the strongest role in determining maneuverability.

For the Y_r and N_r ratios, of figures 4-17a and 4-17b respectively, the ratios follow fairly closely with theory. The Y_r ratio decreases with fin position moving forward, and the ratio of N_r follows a parabolic relationship with fin position, with a minimum when the fin position is around the CoB. With respect to the yaw velocity, r, the flow would not be drastically different at the front of the body in comparison to the back, which could explain why there is no strong descrepency from linearity in the yaw data, like there was in the sway data.

The ratio of added mass terms are exhibited in figure 4-18. Only the $N_{\dot{v}}$ and the $Y_{\dot{r}}$ terms are affected by the fin positon. $Y_{\dot{r}}$ was consistently below the original REMUS's value for all positons. $N_{\dot{v}}$ initially sees an increase in 2.5x from the original REMUS value when the fins were at the far aft location and then sees a destinctive drop, after 0.05 BL ahead of the CoB, to only 2x the original value.

More important, than the individual hydrodynamic coefficient values, is using them to evaluate stability and maneuverability. Following the same format as derived in chapter three, the coefficients were used to compute the stability criterion, C, the Center of Rotational Motion, x_r, the Aerodynamic Center, x_{AC}, and the ratio between x_r and x_{AC}. The results of these computations are listed in table 4.3. The plot of stability index, C, in figure 4-19 follows a similar trend as occurred in the theory of chapter three. The minimum

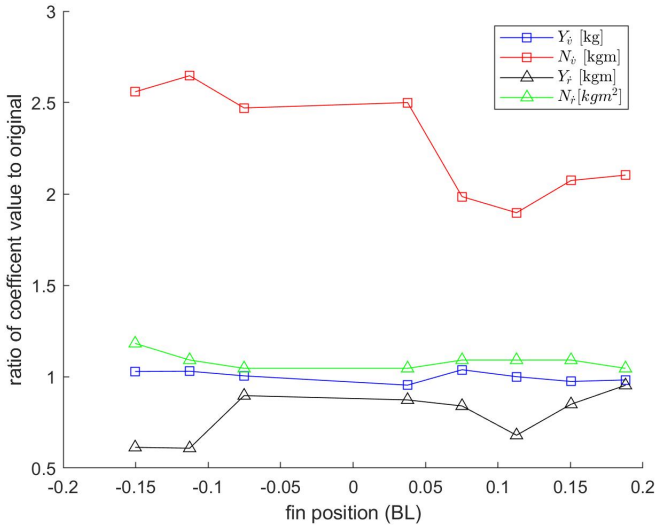

Figure 4-18: Comparing the added mass hydrodynamic coefficients, for each added fin position, to the original REMUS in the form of a ratio to the two

Table 4.3: Stability metrics

fin position [*bodylength*]	C	x_{AC}	x_r	$\frac{x_r}{x_{AC}}$
original REMUS	0.354	0.0593	0.411	8.1706
-0.150	0.818	0.0139	1.686	267.4297
-0.113	0.770	0.0245	1.110	73.0865
-0.075	0.755	0.0253	0.659	34.0933
0.038	0.671	0.0440	0.396	10.8381
0.075	0.688	0.0480	0.383	9.4728
0.113	0.713	0.0557	0.412	8.8731
0.150	0.762	0.0606	0.345	6.5937
0.188	0.780	0.0701	0.284	4.5711

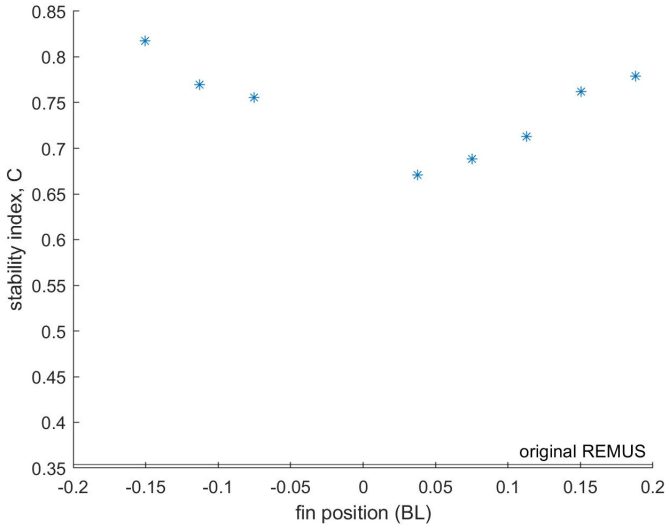

Figure 4-19: The experimental value of the stability index, C, as a function of added fin position. The horizontal line is the experimental value of the original REMUS. For this traditional metric for stability, the smallest positive value indicates the least stable configuration, but is not a desirable method for this type of situation.

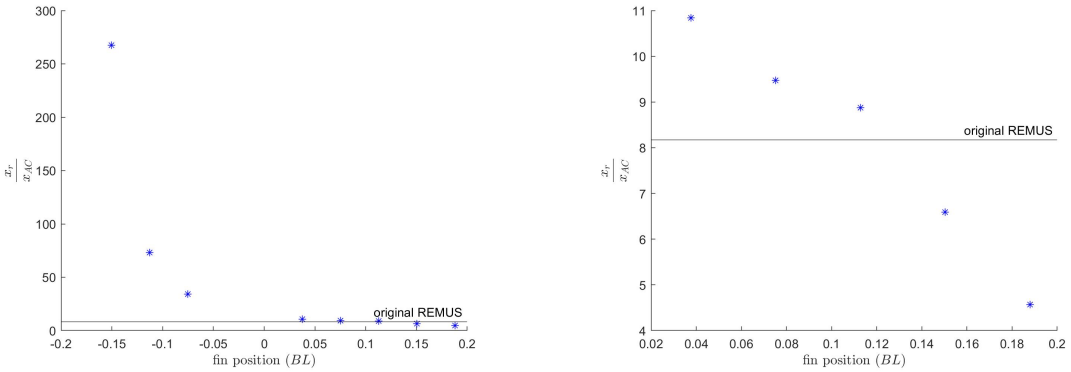

(a) ratio of Center of Rotational Motion, x_r to the Aerodynamic Center, x_{AC}

(b) $\frac{x_r}{x_{AC}}$, focusing on fin position ahead of CoB, C

Figure 4-20: The experimental values of the ratio of Center of Rotational Motion, x_r to the Aerodynamic Center, x_{AC}, as the position of the added fin changes.The horizontal line is the experimental value of the original REMUS. (b) focuses on the fin positions ahead of the CoB, for easier observation of at what fin position $\frac{x_r}{x_{AC}}$ goes below the value of the original REMUS

stability index, C shifted backward slightly, to be between the CoB and 0.03 BL ahead in experiments, as to opposed 0.1 BL as was found theoretically. However, not enough data was collected in this region to determine the critical point. Similarly, Plotting the ratio of x_r to x_{AC} in figure 4-20a, with respect to the added fin position along the hull, corroborates the theoretical findings of chapter three. As was observed in the theoretical calculations, positioning an added fin behind the CoB increases the ratio, which grows exponentially as the fin moves aft. As the fin moves ahead of the CoB, on the other hand, this ratio decreases, and at some point the ratio becomes less than that of the original vehicle. In the theoretical case, this occurred around 0.11 BL. Using figure 4-20b, to hone in on the experimental results for a fin located ahead of the CoB, the ratio passed below the original REMUS value somewhere between 0.11 and 0.15 BL. This is a little more forward on the hull, but not significantly, given there are not enough data points to determine the exact cross-over location. Additionally, the experiments also show a tapering of reduction of the ratio, showing there is a limit to how much can be achieved from the addition of the added fin.

As was seen in chapter three, these two metrics show different results for the supposed maneuverability. The stability criteon indicates that the lowest relative stability and therefore the greatest maneuverability for added fins should occur with fins just ahead of the CoB. However, this vehicle with added fins would still be more stable than the original vehicle. The ratio of x_r to x_{AC}, on the other hand, indicates that the vehicle should become more maneuverable than the original vehicle when the fins are around 0.13 BL ahead of the CoB or greater. These two results are in conflict. Chapter three corroborated with the results of the ratio x_r to x_{AC} as a better metric, through simulations of improved maneuverability with forward fin position. Similarly, the towing tank experiments also indicate that $\frac{x_r}{x_{AC}}$ is a better metric for determining maneuverability for the case of a REMUS with added fins, than the stability index, C. This is because the ratio $\frac{x_r}{x_{AC}}$ follows the trend that was seen with N_v in figure 4-16b, where the coefficient increases rapidly with fin placement, and more so than was expected from theory. As N_v is the most critical coefficient for determining stability, where the larger positive value this coefficient has, the less stable the vehicle is, it is expected this coefficient will indicate when an overall vehicle design is less stable and therefore more maneuverable. Since, the ratio of x_r to x_{AC} exhibits the same trends as N_v for when the critical transition point between the added fin REMUS and the original

REMUS occurs, whereas the stability criterion does not, the ratio of x_r to x_{AC} appears to be a better metric for maneuverability for this case. Using the metric of observing the ratio of x_r to x_{AC}, the REMUS will have an improvement on maneuverability when added fins are placed ahead of the CoB by at least 0.13 BL.

Chapter 5

Vehicle Next Steps

5.1 Critical Rudder Force

The simulations in chapter three and the experiments described in chapter four showed that adding fins towards the aft end of the hull decreased maneuverability, increased stability, and increased the turning radius of the REMUS. This addition of fins to the aft end of the REMUS, is equivalent to having a REMUS without added fins, but with a larger rudder. Relooking at the data with this viewpoint, looking at table 4.3, and comparing the stability coefficient, C, for the REMUS with just the rudder to the case for the REMUS with an added fin at -0.15 BL from the CoB, the stability jumps from 0.354 to 0.818, an increase of 230%, which simulations showed increased the vehicle's turning radius. Given, how adding a fin to the back of the vehicle is similar to just having a larger rudder, it led to the thought that the rudders in the REMUS may actually be too large for the vehicle, adding an unnecessary limitation on the maneuverability. This could explain the modest results of the added fins, since the rudders currently deployed could be too large to be effective for maneuvering, hindering the vehicle from being able to turn adequately.

From this observation, there must be critical amount of force necessary to make the body of the REMUS stable, as rudders are employed in vehicles in order to make the body stable, without making the vehicle too stable. To find this critical rudder coefficient, A_{crit}, one must go back the stability equations of chapter three, remembering, that all of the linear hydrodynamic coefficients used have a component from the body and another from the rudder, as derived in chapter two, and are summarized below

$$Y_v = Y_{v,b} + \frac{Y_\delta}{U} \tag{5.1}$$

$$Y_r = Y_{r,b} - x_{rud}\frac{Y_\delta}{U} \tag{5.2}$$

$$N_v = N_{v,b} - x_{rud}\frac{Y_\delta}{U} \tag{5.3}$$

$$N_r = N_{r,b} - x_{rud}^2\frac{Y_\delta}{U} \tag{5.4}$$

where the body components are denoted by a subscript b next to the coefficient, and the remaining right-hand side term pertains to the rudder. For convenience, Y_δ/U will be relabeled as A. The stability index, C, can now be broken down into its rudder components and body components.

$$\begin{aligned}
C &= -Y_v(mx_GU - N_r) + N_v(mU - Y_r) \\
&= -(Y_{v,b} + A)(mx_GU - (N_{r,b} - x_{rud}^2A)) \\
&\quad + (N_{v,b} - x_{rud}A)(mU - (Y_{r,b} - x_{rud}A)) \\
&= -Y_{v,b}(mx_GU - N_{r,b}) + N_{v,b}(mU - Y_{r,b}) - Y_{v,b}x_{rud}^2A \\
&\quad - A(mx_GU - N_{r,b} + x_R^2A) + N_{v,b}(mU - Y_{r,b}) \\
&\quad + N_{v,b}x_{rud}A - x_{rud}A(mU - Y_{r,b} + x_{rud}A) \\
&= -Y_{v,b}(mU - Y_{r,b})(x_{r,b} - x_{AC,b}) \\
&\quad + A(-mx_GU + N_{r,b} - Y_{v,b}x_{rud}^2 + N_{v,b}x_{rud} + x_{rud}(mU - Y_{r,b}) \\
&= -Y_{v,b}(mU - Y_{r,b})(x_{r,b} - x_{AC,b}) \\
&\quad - A[Y_{v,b}(-x_{rud})(x_{AC,b} - x_{rud}) + (mU - Y_{r,b})(x_{r,b} - x_{rud})]
\end{aligned} \tag{5.5}$$

since the overall stability index, C, must be positive, one can solve for the critical value A_{crit} (in place of A)

$$A_{crit} = \frac{-Y_{v,b}(mU - Y_{r,b})(x_{r,b} - x_{AC,b})}{-Y_{v,b}(-x_{rud})(x_{AC,b} - x_{rud}) + (mU - Y_{r,b})(x_{r,b} - x_{rud})} \tag{5.6}$$

which can be compared to the present rudder force coefficent, A_{rud} of the vehicle,

$$A_{rud} = \frac{Y_\delta}{U} \tag{5.7}$$

to determine the critical size of the rudders. The rudder size is not unique, as there are a number of combinations of spans, chords, and aspect ratios that can produce a valid rudder area. However, for this scope, a rudder area that maintains the same aspect ratio as in the original REMUS will be maintained. From this, the scaling factor, α, of the rudder can be found through

$$\alpha = (\frac{-A_{crit}}{A_{rud}})^{\frac{1}{2}} \tag{5.8}$$

From this equation, the REMUS requires a scaling factor, α, of 0.8468.

5.2 Corrected Simulation

Experiments on the model REMUS were not repeated in the towing tanks, however the simulations performed in chapter three were repeated with the scaling factor, α, applied to the rudders and fins, to observe the differences created. Immediately, from observing figure 5-1a, the turning radius is reduced by 1.6 m for the REMUS with scaled rudders in comparison to the original REMUS. This is a reduction in 20%. The turning radius is also reduced by 1.6 m for every scaled added fin position, in comparison to the originally scaled control fins. Scaling the rudders also shifts the location where the added fin reduces the turning radius from the baseline value forward along the hull. For the originally scaled control surfaces, the crossover point was at around 0.06 BL ahead of the CoB, while for the scaled control surfaces, this occurred at 0.1 BL. From this, the location of fin position, where the added fins improve performance is not constant. It will depend on the vehicle's body design, and the rudder shape. However, it will occur in front of the CoB of the vehicle, for a torpedo shaped UUV.

The optimally scaled control surfaces, as seen in figure 5-1 will come at the cost of the drift angle, β, which is larger in magnitude than for the original scale of the fins, for every fin position. However, when analyzing only the scaled fins with respect to each other, the drift angle, β, follows the same trend seen in chapter three, of the drift angle being reduced

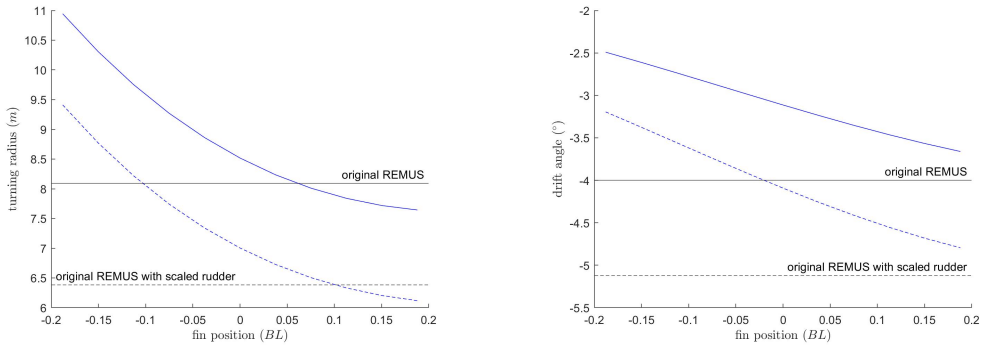

(a) Steady turning radius (b) Steady drift angle

Figure 5-1: Comparing steady state behavior, for critically scaled control surfaces (dotted lines) with the initially sized control surfaces(solid lines) for the REMUS with a pair of added fins placed at different locations on the hull (blue curve), when given a 4° rudder command and 0° fin command to perform a circle maneuver. The horizontal line indicates the baseline value of the REMUS without added fins

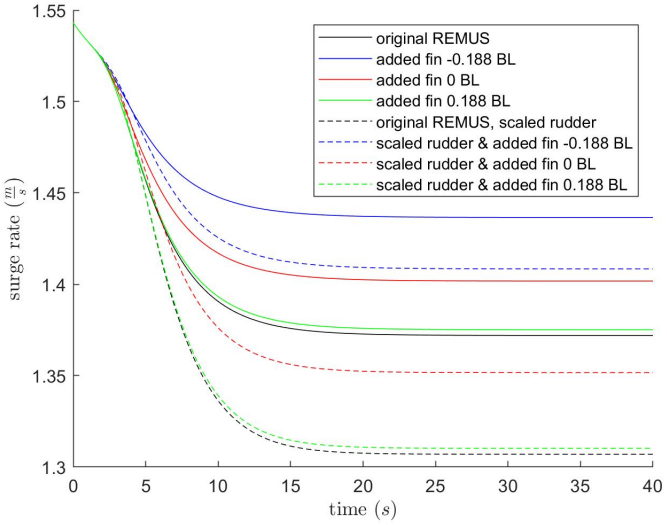

Figure 5-2: Comparing surge velocity behavior of the REMUS, for critically scaled control surfaces (dotted lines) with the initially sized ones (solid lines), during the course of a turn maneuver, when given a 4° rudder command and 0° fin command for select fin cases. Depicted are the REMUS without added fins (black), and fins at furthest aft positon (blue), middle position (red), and furthers forward (green)

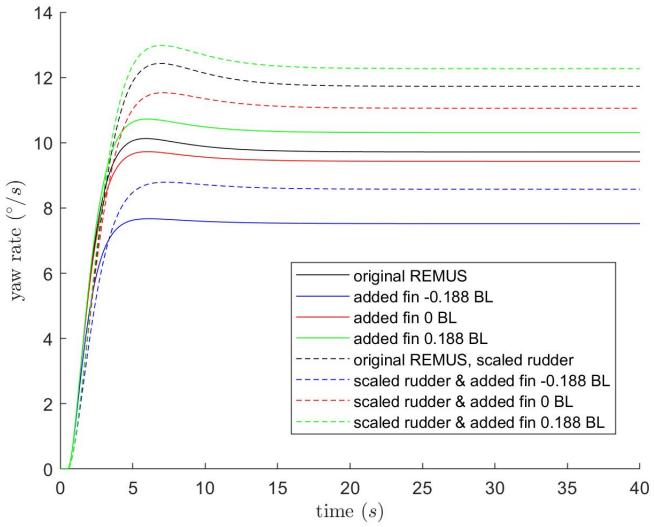

Figure 5-3: Comparing yaw rate behavior of the REMUS, for critically scaled control surfaces (dotted lines) with the initially sized ones (solid lines), during the course of a turn maneuver when given a 4° rudder command and 0° fin command for select fin cases. Depicted are the REMUS without added fins (black), and fins at furthest aft positon (blue), middle position (red), and furthers forward (green)

as the fins move aft on the hull. With a larger drift angle for scaled rudders, the forward speed is reduced in comparison to the original Remus. In figure 5-2, only the case where a scaled fin is located at -0.188 BL, is the speed faster than that of the original REMUS, without scaled rudders. For this case, the yaw rate is slower than the original vehicle as seen in figure 5-3, though for all other cases, the yaw rate is faster. It is worth noting, however, that when the scaled added fins are located between -0.1 BL and 0 BL from the CoB, the drift angle and the turning radius are both reduced, in comparison to the original REMUS without added fins. This shows that there are possible design options for improvement to drift and maneuverability. However, the best improvement for maneuverability is when the fin is located at 0.2 m ahead of the CoB.

5.3 Vehicle Testing

With the completion of simulation and towing tank tests, the next step was to see the behavior of full-scale, functional UUV during missions. A prototype vehicle, of similar type to the REMUS 100 AUV was used for initial full scale vehicle tests. This vehicle had a mass of 9.7031 kg, length of 0.9144 m, and maximum diameter of 0.124 m. Instead of a cruciform

tail like the REMUS, this vehicle had 3 rudders equally space around the tail. This type of vehicle was used due to availability. A pair of rigid fins, affixed to a collar, was 3D printed with PLA, so that the fins could be fixed onto the hull at different locations. Three locations on the hull were picked for testing: the begining of the tail section, the middle of the vehicle, and the end of the nose section. The added fin design and the fin locations are shown in figure 5-4.

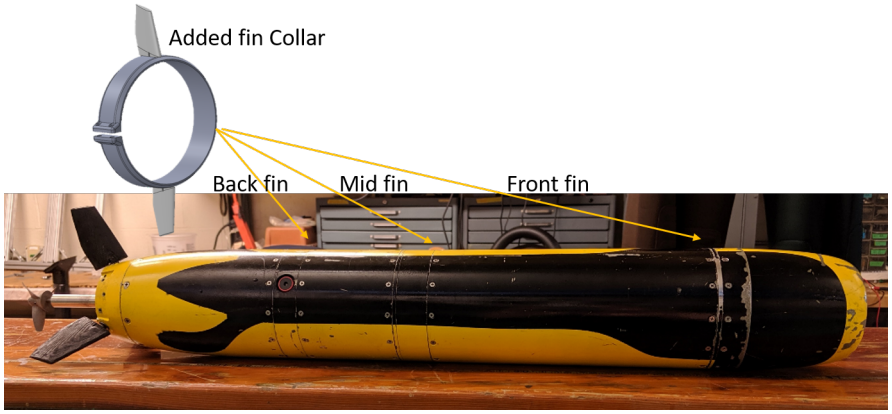

Figure 5-4: Prototype vehicle used for preliminary vehicle tests, with the vehicle's original rudders. Stationary added fins are fixed to the vehicle through a 3D printed collar, at the locations indicated

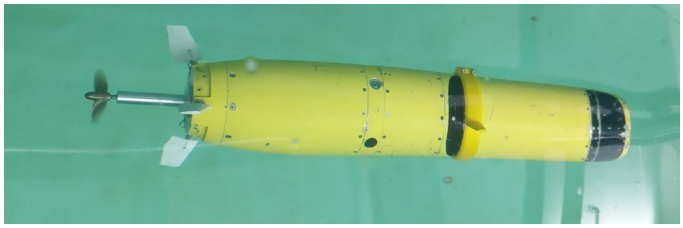

Figure 5-5: Prototype vehicle in the water, with scaled rudders, and with stationary fins added at the mid fin location

With open loop, sensor free design, a zig-zag pattern was programmed into the vehicle. The vehicle was given a command of speed, U, of around 0.6 m/s for 5 seconds, to allow the vehicle to come to steady state. This was followed by a held rudder command of 4° for 3 s, -4° for 6 s, and 4° for 3 s. After this, the rudder was returned to 0° for 3 s before the speed was brought back to 0 m/s.

This vehicle also happened to have oversized rudders, and so scaled down rudders and finis were created. Tests were performed for both, the original rudders and with downscaled

rudders, though for all trials downscaled added fins were utilized. The original, black rudders can be seen adorning the vehicle in figure 5-4, while the downscaled, white rudders can be seen on the vehicle during a test in figure 5-5, which also depicts the added fin midway on the hull. qualitative observational data was collected through video taken by a GoPro affixed to the tank. A summary of the observations are listed in table 5.1.

Table 5.1: Observations of a torpedo shaped vehicle performing an open-loop zig-zag test with added fins

Fin Position	Original Rudders	Scaled Rudders
No Added Fin	Full zig-zag maneuver achieved	Only produced one large turn
Fin Near Tail	Unable to turn	Follows sharp turn in opposite direction from programmed
Fin at Mid-Body	N/A	Performed full zig-zag with same shape as the original vehicle without fins
Fin Near Nose	Performed sharper turn than the original vehicle	Performed sharpest zig-zag maneuver of all variations

For the vehicle with its original rudders, it was able to produce a full zig-zag within the span of the tank, however adding fins near the tail made it so stable, that it was unable to turn. With the fins at the front of the vehicle, it was able to make a sharper turn. A full zig-zag maneuver could not be completed because of the constraints on the size of the tank. When the rudders were downscaled, the vehicle without added fins only managed to complete one turn, as the rudder didn't have enough force for completing a zig-zag in the space. This occurred, because an error in calculation caused the control surfaces to be down-scaled too much, but there was not enough time to fix the scaling. When fins were placed near the tail of the vehicle, the vehicle exhibited an unusual behavior of turning in the opposite direction from what was programmed. Adding fins in the middle or front of the hull caused the vehicle to make subsequently sharper zig-zag motions, showing that the fins were helping the vehicle to maneuver more, despite the undersizing of the control surfaces.

5.4 Next Steps

Further vehicle testing is needed to obtain more quantitative data. Building off of the body of this work, a pair of added fins should be integrated into the hull at approximately 0.2 BL in front of the CoB of a REMUS UUV. This pair of fins should be able to be either fully deployed or compressed into the body, and be able to perform this action multiple times within a mission. During earlier experiments, the transient behavior of the fin deploying was neglected, assuming it would not affect the overall steady state dynamics. However, experiments should be done to confirm this assumption. With full integration of the fins, closed loop control tests of the vehicle running a multitude of the missions, such as zig-zags and full circles should be executed to test the real life behavior of the vehicle, while obtaining position, velocity, and depth data to fully analyze the effects of the fin, and see if there are unwanted memory affects or other such issues that were unable to be analyzed adequately here.

Chapter 6

Conclusion

Underwater vehicles can utilize the same deployable fin mechanism as tunas, in order to be more maneuverable, without requiring a drastic change from standard torpedo shaped, propeller driven designs. Adding a pair of control fins to the hull of a vehicle modulates the stability and therefore the maneuverability of the vehicle. Of particular consequence, as the location of added fins are moved forward along the hull, the ratio of the center of rotational motion, x_r, to the Aerodynamic Center, x_{AC}, reduced, which ended up being a critical metric for determining maneuverability. Observing through simulations, as the ratio decreases, the maneuverability increases, seen through reductions in the turning radius. Static and dynamic towing tank model tests, of a half-scaled REMUS 100 confirmed these results. With further testing on full robotic analogs, control fins placed ahead of the center of buoyancy could be retracted for steady straight motion, and then deployed to allow vehicles to perform tight maneuvers such as rapid turns.

Appendix A

Tables

Table A.1: Table of hydrodynamic coefficients for the REMUS vehicle, derived in chapter two. Not included in the values are the added fin coefficients

Hydrodynamic Coefficient	Units	Value
$X_{\dot{u}}$	kg	-1.5244
X_{prop}	N	6.4467
$X_{u\|u\|}$	$\frac{kg}{m}$	-2.8652
$X_{r\|r\|}$	$\frac{kgm^2}{rad^2}$	-0.9663
X_{vr}	$\frac{kg}{rad}$	32.54
$Y_{\dot{r}}$	$\frac{kgm}{rad}$	0.9663
$Y_{\dot{v}}$	kg	-32.54
Y_{ur}	$\frac{kg}{rad}$	11.4407
$Y_{u^2\delta_r}$	$\frac{kg}{mrad}$	20.5391
Y_{uv}	$\frac{kg}{m}$	-42.3714
$N_{\dot{r}}$	$\frac{kgm^2}{rad}$	-4.3850
$N_{\dot{v}}$	kgm	0.9663
N_{ur}	$\frac{kgm}{rad}$	-9.8019
$N_{u^2\delta_r}$	$\frac{kg}{rad}$	-12.9651
N_{uv}	kg	-8.3723

Table A.2: Table of fitted curve coefficients for $N = av^3 + bv|v| + cv$, from the static experiments performed in chapter four

Fin Position (BL)	a	b	c	R^2
Original REMUS	-18.11	8.101	-0.5222	0.9695
-0.1880	-19.97	8.491	-0.4944	0.9642
-0.1504	-14.27	6.497	-0.351	0.9338
-0.0752	-19.76	8.603	-0.6577	0.9749
0.0376	-19.77	8.658	-0.8474	0.8962
0.0752	-22.00	9.692	-0.9673	0.8867
0.1504	-18.65	8.544	-0.944	0.9164
0.1880	-17.11	8.282	-1.018	0.8876

Table A.3: Table of fitted curve coefficients for $Y = av|v| + bv$, from the static experiments, performed in chapter four

Fin Position (BL)	a	b	R^2
Original REMUS	-24.41	-6.574	0.9797
-0.1880	-12.89	-8.75	0.9531
-0.1504	-16.1	-9.204	0.9797
-0.0752	-27.83	-7.23	0.9887
0.0376	-26.57	-7.96	0.9913
0.0752	-31.88	-7.136	0.9739
0.1504	-20.24	-8.92	0.9628
0.1880	-11.86	-8.433	0.9418

Bibliography

[1] R.W. Blake, L. M. Chatters, and P. Domenici. Turning radius of yellowfin tuna (thunnus albacares) in unsteady swimming manoeuvres. *Journal of Fish Biology*, 46:536–538, 1995.

[2] Mario Paulo Brito, Gwyn Griffiths, and Peter Challenor. Risk analysis for autonomous underwater vehicle operations in extreme environments. *Risk Analysis*, 30(12):1771–1788, 2010.

[3] Erik W. Chapman, Christian Jorgensen, and Molly E. Lutcavage. Atlantic bluefin tuna (thunnus thynnus): a state-dependent energy allocation model for growth, maturation, and reproductive investment. *Canadian Journal of Fisheries and Aquatic Sciences*, 68:1934–1951, 2011.

[4] Paolo Demenici and Robert W. Blake. The kinematics and performance of the escape of the escape response in the angelfish (pterophyllum eimekei). *Journal of Eperimental Biology*, 156:187–205, 1991.

[5] Thor I Fossen. *Guidance and control of ocean vehicles*. Chichester Willey, 1999.

[6] Jeffrey B. Graham Heidi Dewar. Studies of tropical tuna swimming performance in a large water tunnel. *Journal of Experimental Biology*, 192:45–59, 1994.

[7] Sighard F. Hoerner. *Fluid Dynamic Drag*. Published by author, 1965.

[8] Sighard F. Hoerner. *Fluid Dynamic Lift*. Published by author, 1985.

[9] J.N.Newman. *Marine Hydrodynamics*. MIT Press, Cambridge, MA, 1977.

[10] Robert K. Katzschmann, Joseph DelPreto, Robert MacCurdy, and Daniela Rus. Exploration of underwater life with an acoustically controlled soft robotic fish. *Science Robotics*, 3(16), 2018.

[11] Kamran Mohseni. Zero-mass pulsatile jets for unmanned underwater vehicle maneuvering. In *AIAA 3rd" Unmanned Unlimited" Technical Conference, Workshop and Exhibit*, page 6386, 2004.

[12] Vadim Pavlov, Benyamin Rosental, Nathaniel F. Hansen, Jody M. Beers, George Parish, Ian Rowbotham, and Barabara A. Block. Hydraulic control of tuna fins: A role for the lymphatic system in vertebrate locomotion. *Science*, 357(6548):310–314, 2017.

[13] Timothy Prestero. Verification of a six-degree of freedom simulation model for the remus autonomous underwater vehicle. Master's thesis, MIT, 2001.

[14] Michael S Triantafyllou and Franz S Hover. *Maneuvering and Control of Marine Vehicles*. MIT Press, Cambridge, MA, 2002.

[15] Michael S Triantafyllou, Nastasia Winey, Yuri Trakht, Raz Elhassid, and Dana Yoerger. Biomimetic design of dorsal fins for auvs to enhance maneuverability. *Bioinspiration & Biomimetics*, 15(3):035003, 2020.

[16] Junzhi Yu, Min Tan, Shuo Wang, and Erkui Chen. Development of a biomimetic robotic fish and its control algorithm. *IEEE Transactions on Systems, Man, and Cybernetics, Part B (Cybernetics)*, 34(4):1798–1810, 2004.

[17] J. Zhu, C. White, D. K. Wainwright, V. Di Santo, G. V. Lauder, and H. Bart-Smith. Tuna robotics: A high-frequency experimental p;atform exploring the performance space of swimming fishes. *Science Robotics*, 4(34), 2019.